


H2020 MARIE SKŁODOWSKA-CURIE ACTIONS

Smart Mitigation of flow-induced Acoustic Radiation and Transmission for reduced Aircraft, surface traNSport, Workplaces and wind enERgy noise

Grant Agreement No 722401

D1.2 – Interim WP1 report

Source Attenuation: Interim Public Report

Authors: R. Zamponi (VKI), A. Zarri (VKI), T. Suresh (IMP-PAN), C. Teruna (TUD), J. Mohd (TUD), S. Pallejà Cabré (SOTON/ISVR), G. Bampanis (ECL), M. Monfaredi (NTUA), I. Zurbano Fernandez (CETIAT), J. Christophe (VKI)

Due date: December 31st, 2018

Table of Contents

1. Introduction

Sound is a natural mechanism for propagating information, despite the fact that some information are undesired, which are often referred to as noise. Some studies have found correlations between physiological problems with prolonged exposure of noise. Thus, noise pollution is becoming an increasing concern in modern society. Unfortunately, sound production is often the side effect of rapid technological advancement, such as the increased usage of motorized vehicles, electrical generators, ventilation systems, house appliances, and many more. This situation brings forth the necessity to improve our understanding on the underlying physical mechanism of flow-induced noise production, in order to propose feasible noise mitigation strategies.

The SMARTANSWER framework consists of a consortium of 16 research projects to address flow-induced noise mitigation with each of them assigned with an Early Stage Researcher (ESR). This report has been assigned to the task force of WP1 (ESR 1, 2, 6, 7, 8/15, 9, 11, 13, 16) which focuses in noise source attenuation techniques. To this scope, this report is presented as follows:

- An introduction to this document has been presented here
- The contributions of the ESR is presented in the subsequent sections, with a brief literature review of the state-of-the-art and a summary on the present work with preliminary conclusions and the outlook of each project

2. Present Activities of the ESRs on Noise Source Attenuation

2.1. ESR-1: Investigation of turbulence-surface interaction noise mechanisms and their reduction using porous materials

The investigation of the noise generation mechanisms involved in the interaction of a blade profile with incoming turbulence represents a core topic for applications of large societal interest, including airframe noise, aeronautical propulsion systems, HVAC systems for automotive and construction. In these instances, the turbulence is typically produced by elements (such as protection grids, heat exchangers...) that are installed upstream of the airfoil and create inflow distortions. From the physical point of view, sound radiates as a consequence of the rapid changes of the inertia of the turbulent vortexes due to the interaction with the surface of the airfoil. The maximum efficiency occurs in the vicinity of a singular point of the surface, such as a corner or an edge. The sharper the edge, the louder the sound. This is the essence of turbulence impingement noise. Historically, the related phenomenon has been studied by several authors. For example, Paterson and Amiet [1], Migliore and Oerlemans [2] and Moreau et al. [3] demonstrated that turbulence-impingement noise (referred to also as leading edge noise) is predominantly a low-frequency source when the turbulent eddies, related to the acoustic generation, are large scale structures. Moreover, the Amiet theory [4], [5][6] showed that the noise radiation pattern depends on the airfoil compactness with reference to the acoustic wavelength. Additional studies concerning the effect of a real airfoil geometry on the interaction with a turbulent flow can be found in the work of Gill et al. [7], [9] and Kim et al. [8].

The study of the mechanism with whom the turbulence-impingement noise is generated and radiates is instrumental in designing novel sound mitigation approaches. Since acting on the ingested turbulent field is often impossible or anyway challenging in most situations, one promising strategy to reduce the turbulence-impingement noise is to make the acoustic response of the airfoil less sensitive to the turbulent flow. This can be done through geometrical or structural changes of its design or in particular through the usage of absorbing materials. The present report will focus on the latter method and will consider the application of porous materials. The implementation of these materials as part of the structure of the blade has been subject to a number of studies in the past. Roger et al. [[10],[11] filled a NACA-0012 airfoil with steel wool to investigate the leading edge noise reduction in a grid-generated turbulent flow. With the aim of preserving its aerodynamic performances, the core line of the airfoil had been made impenetrable. In this study, porous materials showed to grant a reduction effect with a maximum of 5 dB, even though no optimization of the material parameters had been attempted. Similar designs for a porous airfoil have been adopted also by Sarradj and Geyer [12], Geyer et al. [13], [14], Tinetti [15] and Herr and Reichengerger [16], in the framework of trailing edge noise mitigation. Most of the studies conducted state that the application of these materials may have a significant potential for flow noise mitigation but also that it is necessary to improve the understanding of the influence of the porous material parameters. The already mentioned Sarradj and Geyer [12] focused their analysis on the characterization of this influence by comparing

results of aeroacoustic wind tunnel tests on several porous and non-porous airfoils. They found that not only the overall sound pressure level, but also the spectral characteristics depend on the parameters of the porous material, especially the air flow resistivity. A deeper insight about these correlations should lead to a better comprehension of the physical mechanism responsible for noise reduction, since no agreement about the mode of operation of the porous treatments has been found yet, despite the numerous investigations. Indeed, there are several mechanisms that can be considered responsible for noise reduction [12] and these can be related to acoustic energy absorption by the viscous and thermal losses occurring during the oscillatory fluid motion in the pores of a porous material or to dissipation of turbulent energy from the boundary layer by the porous surface. With regard to turbulence-impingement noise, one possible mitigation mechanism may be represented by the reduction of the time variation of the inertia of the turbulent vortexes due to the possibility for part of the incident velocity to penetrate the material [11].

The objective of this document is to describe the implementation of a porous material, and in particular melamine foam, in a NACA-0024 airfoil for the investigation of turbulence-impingement noise conducted at *von Karman Institute for Fluid Dynamics* (VKI). The approach that has been adopted for its composition is similar to the one of Roger et al. [[10],[11], already discussed. The porous profile has been designed with a chord of 0.157 m, corresponding to a maximum thickness of 3.77 mm, and a span of 0.200 m. The choice of the chord has been made in order to ease the manufacturing and the instrumentation of the model. For the purpose of avoiding cross-flow between the two sides of the profile, the center plane has been made solid. The volume of the airfoil has then been filled with melamine foam, selected because easy to cut to a desired shape. A porous hard plastic exo-skeleton has the function to contain the foam and to ensure the proper shape fidelity. It is made of two components, one per each side of the airfoil surface, that are assembled on the solid centerplane and glued in correspondence of the leading edge and the trailing edge. The same manufacturing technique has been adopted to produce the solid airfoil. In this case the exo-skeleton does not present any porosity. All the profiles have been finally coated with the same metallic wire mesh, which protects the materials and guarantees a good surface roughness quality. Ideally this envelope should minimize the viscous losses in the boundary layers and allow for fluid penetration into the inner porosity of the porous airfoil. In Figure 1a a scheme illustrating the different parts constituting the porous airfoil is depicted, whereas in Figure 1b a photograph of the two manufactured prototypes is shown.

(a) **(b)**

Figure 1: (a) Scheme of the porous NACA-0024 used in the experiments. (b) Comparison between the manufactured porous airfoil (on the left) and the solid one (on the right)

In order to perform static pressure distribution and wall pressure fluctuations measurements, two different versions of the NACA-0024 have been manufactured per each configuration. One of these is equipped with 35 static pressure sensors, whereas the other one with 35 microphones placed at the same positions. In each surface there are 17 transducers at the midspan that correspond to the 1.4%, 3.4%, 5.7%, 8.4%, 12.5%, 16.7%, 21.0%, 26.7%, 32.4%, 38.1%, 49.5%, 55.2%, 60.9%, 66.5%, 72.6% and 77.8 % of the chord. An additional measurement position has been considered in correspondence to the leading edge.

As mentioned above, the parameters of the porous medium play an important role in the investigation of the noise reduction mechanisms and for this reason a particular emphasis has been put on their characterization. According to the Johnson-Champoux-Allard-Lafarge (JCAL) model, six parameters are necessary to fully characterize the material. These include:

- The air flow resistivity, σ, which corresponds to the ratio of a pressure difference Δp across a sample of porous material in the presence of a static fluid flow through it to the product of the flow velocity v and the sample thickness d, relationship known also as Darcy's law [17].
- The porosity, φ, which is defined as the ratio between the accessible pore volume - since those pores which are closed and not accessible are not expected to have an influence on the acoustical and aerodynamical characteristics - and the total volume;
- The tortuosity, α_∞, which takes into account the sinuous fluid paths through the porous material;
- The viscous characteristic length, Λ, introduced by Johnson et al. [18], which considers the medium and high frequency viscous and inertial effects;
- The thermal characteristic length, Λ', defined by Champoux and Allard [19], which expresses the thermal exchanges between the material frame and the pore saturating fluid at medium and high frequencies;
- The thermal permeability, k_0', introduced by Lafarge et al. [20], which models the thermal exchanges between the porous material frame and the saturating fluid at low frequencies.

Another parameter that can be used to define a porous medium is the viscous permeability, k_0, which is directly linked to σ. Indeed, it is defined as the ratio of the dynamic viscosity of air to the static air-flow resistivity.

The characterization of these quantities has been performed in collaboration with *Laboratoire d'Acoustique de l'Université du Maine* (LAUM). For their estimation, an inverse method based on the measurement of the melamine foam scattering matrix by means of a 4-microphones impedance tube has been considered [21]. This technique consists of fitting a model which describes the porous medium to the measurement. The inversion is done in the Bayesian framework, whereas the model used for the porous media is the JCAL one. The results of the characterization are listed in Table 1. The estimation can be considered reliable, since a good

match has been found with previous results from ultrasonic measurements conducted on the same sample and not discussed in this report.

Table 1: JCAL model parameters characterizing the melamine foam of the porous airfoil.

σ [Pa· s · m^{-2}]	φ [-]	α_∞ [-]	Λ [m]	Λ'[m]	k_0 [m^2]	k_0' [m^2]
12,835.7	0.986	1.02	1.344×10^{-4}	1.942×10^{-4}	1.410×10^{-9}	2.382×10^{-9}

Considering the parameters of the hard plastic exo-skeleton and the metallic wire mesh, the first has been designed to have $\varphi = 80\%$, whereas the second to have $\varphi = 60.8\%$. Air flow resistivity measurements have been performed at *Centre de Transfert de Technologie du Mans* (CTTM), in Le Mans, with samples of the two materials. As expected, the σ of the two layers was negligible. This confirms the fact that the air flow resistivity of the porous airfoil is governed by the one of the melamine foam.

Concerning the evaluation of the performances of the porous airfoil in terms of noise reduction, the experimental setup which will be used for the investigation consists of a rod-airfoil configuration, already used by de Santana [22]. A scheme of the setup is shown in Figure 2. In this arrangement, the wing profile undergoes a broadband perturbation that is dominated by a preferred shedding frequency, similarly to what can be observed in most turbo-machinery applications [23]. Moreover, as stated by Roger and Moreau [11], the analysis of the turbulence-impingement noise reduction that is possible to obtain with the use of porous treatment provides similar results for a rod-airfoil and a tandem airfoil configuration.

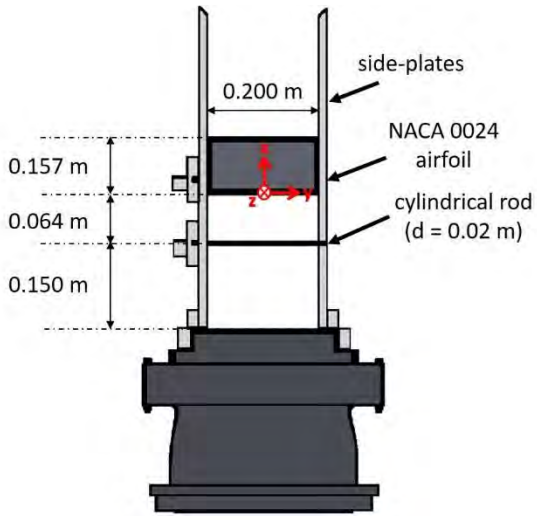

Figure 2: Scheme of the rod-airfoil configuration.

A first comparison of the performances of both solid and porous airfoil will be carried out at one angle of attack and one flow velocity. The boundary layers around the profiles will be characterized by means of hot-wire anemometry and the analysis of the static pressure distribution and the wall pressure fluctuations along their surfaces. Acoustic far-field measurements and Generalized Inverse Beamforming (GIBF) [24],[25] will be finally applied to study the noise reduction achievable by the use of a porous treatment of the airfoil.

2.1.1. References

[1] Paterson, R. W., Amiet, R. K., "Acoustic radiation and surface pressure characteristics of an airfoil due to incident turbulence", Tech. rep., National Aeronautics and Space Administration, 1976.

[2] Migliore, P., Oerlemans, S., "Wind tunnel aeroacoustic tests of six airfoils for use on small wind turbines", Tech. Rep. NREL/CP-500-35090, National Renewable Energy Laboratory, 2003.

[3] Moreau, S., Roger, M., Jurdic, V., "Effect of angle of attack and airfoil shape on turbulence-interaction noise", 11th AIAA/CEAS Aeroacoustics Conference (26th AIAA Aeroacoustics Conference), 2005.

[4] Amiet, R., "Acoustic radiation from an airfoil in a turbulent stream", Journal of Sound and Vibration 41, vol. 4, pp. 407 – 420, 1975.

[5] Amiet, R. K., "Effect of the incident surface pressure field on noise due to turbulent flow past a trailing edge", Journal of Sound and Vibration 57, vol. 2, pp. 305 – 306, 1978.

[6] Amiet, R. K., "Noise due to turbulent flow past a trailing edge", Journal of Sound and Vibration 47, vol. 2, pp. 387 – 393, 1976.

[7] Gill, J. R., Zhang, X., Joseph, P., "Effects of Real Airfoil Geometry on Leading Edge Gust Interaction Noise," American Institute of Aeronautics and Astronautics, 2013.

[8] Kim, D., Lee, G.-S., Cheong, C., "Inflow broadband noise from an isolated symmetric airfoil interacting with incident turbulence," *Journal of Fluids and Structures*, vol. 55, pp. 428–450, May 2015.

[9] Gill, J., Zhang, X., Joseph, P., "Symmetric airfoil geometry effects on leading edge noise", *The Journal of the Acoustical Society of America,* vol. 134, pp. 2669–2680, 2013.

[10] Roger, M., Schram, C., de Santana, L., "Reduction of Airfoil Turbulence-Impingement Noise by Means of Leading-Edge Serrations and/or Porous Material", American Institute of Aeronautics and Astronautics, 2013.

[11] Roger, M., and Moreau, S., "Airfoil Turbulence-Impingement Noise Reduction by Porosity or Wavy Leading-Edge Cut: Experimental Investigations," InterNoise16, Hamburg, DE, 2016.

[12] Sarradj, E., Geyer, T., "Noise generation by porous airfoils," *13th AIAA/CEAS Aeroacoustics Conference Proceedings, AIAA*, 2007.

[13] Geyer, T., Sarradj, E., Fritzsche, C., "Porous airfoils: noise reduction and boundary layer effects", International journal of aeroacoustics, vol. 9, pp. 787–820, 2010.

[14] Geyer, T., Sarradj, E., and Fritzsche, C., "Measurement of the noise generation at the trailing edge of porous airfoils," Experiments in Fluids, Vol. 48, No. 2, 2010, pp. 291–308.

[15] Tinetti, A. F., "On the Use of Surface Porosity to Reduce Wake-Stator Interaction Noise," Ph.D. thesis, Virginia Tech, Sep. 2001.

[16] Herr, M., and Reichenberger, J., "In Search of Airworthy Trailing-Edge Noise Reduction Means", American Institute of Aeronautics and Astronautics, 2011.

[17] Scheidegger, A., The Physics of Flow Through Porous Media, University of Toronto Press, 1963.

[18] Johnson, D. L., Koplik, J., and Dashen, R., "Theory of dynamic permeability and tortuosity in fluid-saturated porous media," Journal of Fluid Mechanics, Vol. 176, 1987, pp. 379–402.

[19] Champoux, Y., and Allard, J., "Dynamic tortuosity and bulk modulus in air-saturated porous media," Journal of Applied Physics, Vol. 70, No. 4, 1991, pp. 1975–1979.

[20] Lafarge, D., Lemarinier, P., Allard, J. F., and Tarnow, V., "Dynamic compressibility of air in porous structures at audible frequencies," The Journal of the Acoustical Society of America, Vol. 102, No. 4, 1997, pp. 1995–2006.

[21] Niskanen, M., Groby, J.-P., Duclos, A., Dazel, O., Le Roux, J. C., Poulain, N., Huttunen, T., and Lähivaara, T., "Deterministic and statistical characterization of rigid frame porous materials from impedance tube measurements," The Journal of the Acoustical Society of America, Vol. 142, No. 4, 2017, pp. 2407–2418.

[22] De Santana, L., "Semi-analytical methodologies for airfoil noise prediction", KU Leuven, 2015.

[23] Lorenzoni, V., Tuinstra, M., and Scarano, F., "On the use of time-resolved particle image velocimetry for the investigation of rod–airfoil aeroacoustics," Journal of Sound and Vibration, Vol. 331, No. 23, 2012, pp. 5012–5027.

[24] Zamponi, R., de Wyer, N. V., and Schram, C., "An Improved Regularization of the Generalized Inverse Beamforming Applied to a Benchmark Database," 7th Berlin Beamforming Conference, BeBeC, Berlin, DE, 2018.

[25] Zamponi, R., Van de Wyer, N., and Schram, C. F., "Benchmark Assessment of an Improved Regularization Technique for Generalized Inverse Beamforming," 2018 AIAA/CEAS Aeroacoustics Conference, American Institute of Aeronautics and Astronautics, Atlanta, Georgia, 2018.

2.2. ESR-2: Flow and acoustic control for automotive low-speed cooling fans

The contribution given to D1.2, through the Task 1.2, is aimed at describing the modelling of the micro-perforated plates (MPPs) employed as sound absorbing material. The author refers to his previous contribution on D2.1 Task 2.1, to have a first overview of the possible MPPs applications. An example of which, the work of Allam and Abom [1] regarding the noise reduction of an automotive radiator cooling fan achieved with the use of MPPs, showed the potential of this technology when applied to rotational cooling machinery. In the following sections, the MPPs will be firstly described from their physical point of view and then, the classical modelling methodologies will be discussed along with the main problems which are still matter of research.

2.2.1. Micro-perforated plates modelling review

Perforated plates are plates on the surface of which orifices of generic shape, typically slits or circular holes, are engraved. As in porous or fibrous materials, the aim is to convert acoustic energy into heat. This is carried out by the friction between the oscillating air particles against the internal and external parts of the holes, as well as by exploiting the resonance properties of the backing cavity [2]. Therefore, to employ them as useful sound absorbing materials, the oscillating viscous boundary layers (Stokes layers) have to fill up almost completely the volume of the holes. This is obtained by keeping the dimensionless Shear number (k) approximately equal to 1. To define k, a relation between the hole characteristic dimension $(d/2)$ with respect to the viscous boundary layer thickness $(\sqrt{\nu/\omega})$ is shown as $k = d\sqrt{\omega/4\nu}$, where the kinematic viscosity of the acoustic medium (ν) and the radian frequency of the sound excitation (ω) are present. Hence, micro-perforated plates with tens of thousands of sub-millimeter orifices are required and they need to have a porosity (σ), defined as the open area with respect to the plate surface ratio, in the order of 1%. This is instrumental in increasing the particle velocity level within the orifice, in order to have a more efficient viscous dissipation. Generally, the thickness of an MPP (t) is normally chosen so that the ratio (t/d) is kept in the order of 1.

2.2.2. MPPs modelling

As Maa stated in [3], a MPP is defined as a surface with controlled complex impedance Z_{MPP} where the real part, called resistance R_{MPP}, has to be constant (frequency-independent), while the imaginary part, the reactance M_{MPP}, has to be small enough such that $Z_{MPP} = R_{MPP} + j\omega M_{MPP} \approx \rho c$, (being ρc the characteristic impedance of the air, with the density ρ and the speed of sound c). The viscous effects are represented by the acoustic resistance, while the reactance represents the air inertia to be moved by the acoustic waves. The absorption peak is therefore perfectly retrieved when the imaginary part is ideally equal to zero, while the resistance is equal to the air characteristic impedance, at that particular frequency. This is required so that the maximum amount of acoustical energy can enter the orifice without encountering a jump of impedance. To control at which frequency the absorption peak appears, it is possible to tune the air cavity depth (L_c), such that a behavior similar to a Helmholtz resonator is achieved. Nevertheless, a classical resonator reaches a good sound mitigation only at its resonance frequency, since the viscous effects are negligible. Instead, for the MPPs, the absorption range has a broadband spectrum due to the dissipation mechanisms within and near to the orifices. To

further enlarge the absorption range, one may consider to adopt multi-layer MPPs, as well as to subdivide the backed air cavity, for instance, with honey-combs, in order to increase the local reaction to the acoustic waves [4]. Nevertheless, only single-layer with air cavity are considered hereafter.

2.2.3. Dissipation mechanisms

When one considers the acoustical impedance of a micro-perforated plate, different dissipation mechanisms have to be taken into account: the thermal effects, the radiation, the viscosity, the flow interaction and the non-linearity due to high sound levels. The first two can be neglected as stated in [2] and later confirmed in [5].

2.2.4. Internal viscous contribution

The contributions given by viscosity to the MPP transfer impedance can be separately considered as internal and external parts. The first one is due to the oscillating viscous boundary layers inside the orifice volume. From the theory of sound propagation in tubes, developed by Lord Rayleigh [6] and simplified by Crandall [7] for short tubes, the equation of air motion inside a single cylindrical orifice is given by:

$$j\omega\rho u - \frac{\nu}{r}\frac{\partial}{\partial r}\left(r\frac{\partial}{\partial r}\,u\right) = \frac{\Delta p}{t} \tag{1}$$

being Δp the sound pressure difference between the ends of the tube, u the particle velocity and r the hole radius. The solution can be written defining the single-hole impedance (Z_1) as the ratio between Δp to the averaged cross-sectional averaged velocity ($\bar{u}$) as:

$$Z_1 = \frac{\Delta p}{\bar{u}} = j\omega\rho t\left[1 - \frac{2}{k\sqrt{-j}}\frac{J_1\left(k\sqrt{-j}\right)}{J_0\left(k\sqrt{-j}\right)}\right]^{-1} \tag{2}$$

where J_0 and J_1 are the Bessel functions of the first kind of zero and first order respectively.

Eq. (2) can be easily normalized by the air characteristic impedance and extended to the MPPs relative acoustic impedance by dividing it by the porosity:

$$z_{in} = \frac{j\omega t}{\sigma c}\left[1 - \frac{2}{k\sqrt{-j}}\frac{J_1\left(k\sqrt{-j}\right)}{J_0\left(k\sqrt{-j}\right)}\right]^{-1} \tag{3}$$

being z_{in} the relative acoustic impedance due to internal viscous effects.

A similar solution for slit-shaped perforated plates has been derived by Allard [8], but it is not here reported, for the sake of simplicity.

For circular-shaped holes, Maa [2] derived the following expression for the internal resistance r_{in} of an orifice invested by a perpendicularly incident sound wave:

$$r_{in} = \frac{32\nu}{\sigma\rho c}\frac{t}{d^2}\sqrt{1+\frac{k^2}{32}} \tag{4}$$

while for the reactance part (m_{in}):

$$m_{in} = \frac{t}{\sigma c}\left(1+\frac{1}{\sqrt{1+\frac{k^2}{2}}}\right) \tag{5}$$

2.2.5. External viscous contribution

Since thin plates are studied, the external shape-dependent viscous dissipation developing on the orifice ends have to be modelled. Ingard [9] suggested that from the power dissipation occurring to oscillating air motion on an infinite plane surface (S), approximately given by:

$$W_v = \frac{1}{2}\int_S R_S|U_S|^2 dS \tag{6}$$

with U_S as the tangential velocity amplitude, the "surface resistance" can be expressed as:

$$R_S = \frac{1}{2}(2\mu\rho\omega)^{\frac{1}{2}} \tag{7}$$

being μ the dynamic viscosity. A motion of air mass occurs next to the orifice edges and therefore, a contribution to the reactance has been theoretically calculated by Crandall [7] and Sivian for circular holes [10] as $\delta = 8d/3\pi$. Globally, the external contribution to the relative impedance for an MPP can be written as:

$$z_{ex} = \frac{\alpha 2R_S}{\sigma\rho c} + j\frac{\delta\omega}{\sigma c} \tag{8}$$

where α is a factor which is equal to 2 for rounded orifice ends and to 4 for sharp ones [11]. Nevertheless, as Ingard based his end-correction coefficient derivation on plane surfaces, when the curvature radius of the perforation edge is small, this formulation can occur in serious problems. To solve this, a numerical model in 2D axisymmetric coordinates has been developed by Bolton and Kim [12] and generalized, for circular perforations in linear regime, with an analogous method by Muttalip *et al.* [13]. In this work, different circular edge profiles were studied such as square, chamfered, inverse-chamfered and their linear combinations. It is shown that, while plate thickness has a negligible effect on the end-correction coefficients, α and δ strongly depend on k number, thus they are frequency-dependent, and on the edge profile. For instance, for the square-edge profile case, which is comparable to theory, asymptotic values are found with increasing k as $\alpha = 1.70$ and $\delta = 1.54$. For chamfered profile, both α and δ are increased since internal-hole friction region is reduced, considering the same plate thickness.

Therefore, the two coefficients have been expressed as functions of k and the edge-profile, fitting the experimental results.

2.2.6. Non-linear contribution

Non-linear dissipation effects occur when the acoustic particle velocity within the orifice reaches high values due to moderate to high sound intensity levels [14]. In this condition, flow separation and vortices appear on the hole edges in a free-jet configuration, becoming an important part of the acoustic resistance. In fact, the developed vorticity is alimented by converting the acoustic field energy. Even the reactance is decreased and, although this process is not fully understood [15] [11], this is likely due to the turbulent-jet breaking apart the slug of mass present in and around the orifice region. An interesting conclusion is reported in the work of Leung *et al.* [16], since they noticed how the vortices are typically shed upstream and downstream of the orifice, but they are shed only downstream when a bias flow is present. To understand when the non-linear formation of vortices starts, the study can be based on the Strouhal number [17]:

$$Sr = \frac{\omega d}{|\bar{u}|} \tag{9}$$

If $Sr \gg 1$, the vortices do not normally appear since the particle displacement is smaller than the hole diameter and thus, the system is linear and no other contribution is added to the impedance. If $Sr \gg 1$, the non-linear turbulent jet is totally developed; for this case, Cummings and Eversman [18], assuming quasi-steady behavior, derived the particle velocity from the Bernoulli equation. With the assumption of negligible downstream pressure past the orifice, the upstream acoustic pressure amplitude is given by:

$$|p_{up}| \approx \rho |u_h|^2 \, \frac{1 - \sigma^2 C_v^2}{2 C_v^2} \tag{10}$$

where $|u_h|$ is the amplitude peak of the velocity within the hole, while C_v is the *vena-contracta* factor, which is geometry-dependent and, for sharp edges, is $C_v \approx 0.7$. Moreover, due to MPPs low porosity levels, the term $\sigma^2 C_v^2 \approx 0$. For these reasons, the initially proposed formula by Ingard and Ising [19] is applicable to sharp-edges, leading to the resistance non-linear contribution:

$$r_{n-l} = \frac{|u_h|}{\sigma c} \tag{11}$$

For the reactance part, an empirical formula has been proposed by Maa [14] to be multiplied to the end correction term: $\delta(1 + r_{n-l})^{-1}$.

Nevertheless, these relations are valid when the behavior is fully non-linear, *i.e.*, $Sr \gg 1$. To fulfill the transition regime between linearity and non-linearity, Temiz *et al.* [17] provided correction functions for resistance and reactance, which are strongly dependent on the Shear and the Strouhal numbers and can be used for practical MPPs design. It is important to highlight though, that these terms are dependent also on the kind of perforation. In fact, as shown by

Temiz *et al.* [20] for instance, compared to square-edge profiles, for the chamfer-edge profiles the non-linear resistance contribution is decreased of around 50%.

2.2.7. Flow interaction contribution

For rotational machinery applications, it is also important to take into account the impedance contribution due to the presence of a tangential flow parallel to the MPP plane referred to as grazing flow. To the acoustic resistance, according to the work of Åbom and Allam [21], a term proportional to the Mach number (M) of the grazing flow has to be added: $\beta M/\sigma$, being $\beta = 0.15$ for MPPs with circular holes. Guo *et al.* [11] showed that it depends on the slit orientation for slit-edge perforations. Furthermore, the presence of the flow blows away the air mass at the orifice ends; for this reason, the mass end correction has to be corrected. The relation between the mass end correction with no flow (δ) and the one with the grazing flow (δ_g) is given by Rice [22] as:

$$\delta_g = \frac{\delta}{1 + \alpha_g M^3} \tag{12}$$

being $\alpha_g = 305$, although further analysis carried out in [11], showed that a factor of 6-7 has to be multiplied to α_g for the tested MPPs.

2.2.8. MPP absorbing coefficient and cavity depth length

For normal acoustic incidence, the absorption coefficient (α_{MPP}) of a micro-perforated plate with a backed cavity, is given by [2] as:

$$\alpha_{MPP} = \frac{4r}{(1+r)^2 + (\omega m - \cot(\omega L_c/c))^2} \tag{13}$$

where the relative acoustic resistance of the cavity is $-\cot(\omega l/c)$. The maximum value of α_{MPP} is $\alpha_0 = 4r/(1+r)^2$, occurring at the resonance frequency (f_0) for which:

$$\omega_0 m - \cot\left(\frac{\omega_0 L_c}{c}\right) = 0 \tag{14}$$

with $f_0 = 2\pi\omega_0$. In a practical application context, from the solution of the equation above the cavity length (L_c) can be deduced in order to tune the MPP at the resonance frequency:

$$\frac{L_c}{\lambda} = \frac{1}{2\pi}\cot^{-1}(\omega_0 m) \tag{15}$$

where $\lambda = c/f_0$ is wavelength corresponding to the resonance frequency.

The resistance (r) and reactance (m) parts of the relative transfer acoustic impedance of a MPP with circular sharp-edge orifices, can be finally written collecting the previously derived contributions of viscous, flow-interaction and non-linear effects as:

$$r = \frac{1}{\rho\sigma c}\left(32\nu\frac{t}{d^2}\sqrt{1+\frac{k^2}{32}} + 2\alpha R_S + |u_h|\rho + \beta M\rho\sigma c\right)$$

(16)

$$m = \frac{t}{\sigma c}\left(t\left(1+\frac{1}{\sqrt{1+\frac{k^2}{2}}}\right) + \frac{\delta\omega(1+r_{n-l})^{-1}}{1+\alpha_g M^3}\right)$$

2.2.9. Conclusions

The micro-perforated plates have been chosen as promising sound mitigation technology to be applied to automotive low-speed cooling fans. In fact, within the hood of cars for instance, clean, durable, not-cumbersome, temperature and moist resistant solutions are desirable. The dissipation effects, including viscosity, flow interaction and non-linearity occurring on MPPs have been analyzed and modelled. Hence, guidelines have been traced for designing a new MPP prototype tuned to absorb parts of a typical sound spectrum emitted by low-speed cooling fans. Nevertheless, many parameters contribute to the calculation of the MPP transfer acoustic impedance, as well as the absorbing coefficient and for this reason, an optimization technique will be likely needed to find the most suitable solution.

2.2.10. References

[1] Allam, S., Abom, M., "Noise reduction for automotive radiator cooling fans," *Conference Paper Fan2015,* Lyon, 2015.

[2] D.-Y. Maa, "Potential of micro-perforated panel absorber," J. Acoust. Soc. Am., vol. 104, no. 5, pp. 2861–2866, 1998.

[3] Maa, D. Y., "Theory and design of a micro-perforated plate absorption structure," *China Sci. 1:38-50* [in Chinese], 1975.

[4] Allam, S. and Abom, M., "A New Type of Muffler Based on Micro-Perforated Tubes," J. Vib. Acoust. 133:031005-1-031005-6, 2011.

[5] T., Herdtle and J. Stuart Bolton, "Effect of Thermal Losses and Fluid-Structure Interaction on the Transfer Impedance of Micro-Perforated Films," Proceedings of Noise-Con 2014, Fort Lauderdale FL, 12 pages, 2014.

[6] Lord Rayleigh, *Theory of Sound II* (MacMillan, New York, 1929 ed.), p.327

[7] I. B., Crandall, *Theory of Vibration System and Sound* (Van Nostrand, New York, 1926), pp. 229 et seq.

[8] J.F., Allard. “Propagation of sound in porous media modelling sound absorbing materials” London, Elsevier Applied Science, cop. 1993.

[9] U., Ingard, “On the theory and design of acoustics resonators” *Journal of the Acoustical Society of America.* Vol. 25,1044, (1953).

[10] L., J., Sivian. “Acoustic Impedance of small Orifices”, *Journal of the Acoustical Society of America,* Vol. 7, 1935.

[11] Y. Guo, S. Allam, and M. Åbom, “Micro-perforated plates for vehicle application,” in The 37th International Congress and Exposition on Noise Control Engineering, (Beijing, China), pp. 773–792, 2009.

[12] J. S. Bolton and N. Kim, “Use of CFD to Calculate the Dynamic Resistive End Correction for Microperforated Materials,” Acoustics Australia, vol. 38, no. 3, pp. 134–139, 2010.

[13] Muttalip, A., T., Lopez Arteaga, I., Efraimsson, G., Åbom, M. and Hirschberg, A. (2015) “The influence of edge geometry on end-correction coefficients in micro perforated plates”. J. Acoust. Soc. Am. 138 (6).

[14] D. Y. Maa, “Micro-perforated panel at high sound intensity,” in Proceedings of Internoise 1994, vol. 94, (Yokohama), pp. 1511–1514, 1994.

[15] K. K., Ahuja and R. J. Gaeta, *Jr.* “Active Control of Linear Impedance by Varying Perforate Orifice Geometry” Georgia Institute of Technology, Atlanta, Georgia *NASA/CR-2000-210633.*

[16] R. C. K. Leung, R. M. C. So, M. H. Wang, and X. M. Li, “In-duct Orifice and Its Effect on Sound Absorption,” Journal of Sound and Vibration, vol. 299, pp. 990–1004, 2007.

[17] M. A. Temiz, I. Lopez Arteaga, G. Efraimsson, M. Åbom, and A. Hirschberg, “Acoustic end correction in micro-perforated plates - revisited,” in 21st International Congress on Sound and Vibration 2014, ICSV 2014, vol. 2, (Beijing), pp. 1203–1209, 2014.

[18] A. Cummings and W. Eversman, “High amplitude acoustic transmission through duct terminations: Theory,” The Journal of Sound and Vibration, vol. 91, no. 4, pp. 503–581, 1983.

[19] U. Ingard and H. Ising, “Acoustic Nonlinearity of an Orifice, The Journal of the Acoustical Society of America, vol. 42, no. 1, pp. 6–17, 1967.

[20] M. A. Temiz, J. Tournadre, I. Lopez Arteaga, and A. Hirschberg, “Non-linear acoustic transfer impedance of micro-perforated plates with circular orifices, Journal of Sound and Vibration, vol. 366, pp. 418–428, 2016.

[21] S., Allam and M., Åbom. “Experimental Characterization of Acoustic Liners with Extended Reaction”, *14th AIAA/CEAS Conference,* 2008-3074.

[22] E. J., Rice. “Acoustic aerodynamic performance of a 6-foot-diameter fan for turbofan engines, III-performance with noise suppressors”, *NASA TN- D 6178,* 1971.

2.3. ESR-6: Separation and wake noise reduction by means of streamwise vortex generators

Flow control devices are extensively used in various industries to limit the flow separation and to reduce its adverse effects on the performance of the machines. They are designed to tackle the problems of boundary layer growth. With years of research many active and passive control devices have been developed, tested and implemented, each suiting specific industries. One such device is the vortex generators. The idea of vortex generator (VG) was developed in 1946 by the wind tunnel group of the United Aircraft Corporation for a project on eliminating boundary layer separation in the first diffuser of their wind tunnel [1]. Historically they are known as an aerodynamic "band-aid" to deal with localized mach buffet problems at the high end of the airspeed envelope.

The vortices created by VGs transfer low energy fluid from the surface into the free-stream and brings higher energy fluid from the free-stream down to the surface where the higher kinetic energy level is able to withstand a greater pressure rise before separation occurs. VGs also excite local instability waves that causes early transition to turbulence thus delaying flow separation and reduces the size of the separation zone. Detailed studies on VGs and their effects on the boundary-layer is performed by Schubauer and Spangenberg [2]. Extensive studies on passive VG for low profiles with different design parameters is conducted by Lin [3]. To overcome complicated usage of sophisticated VGs in applications like different flow regimes of helicopters and wind turbines, a novel design called Rod vortex generator (RVG) was developed by Doerffer P et al [4]. Both computational and experimental analysis for the RVG and the air jet type of vortex generators in channel flows is available in [5], [6]. Further aerodynamic enhancement of the profile was conducted by Tejero et al [7]. Exhaustive simulations for the analysis of RVGs on wind turbines is available in Martinez's doctoral thesis [8].

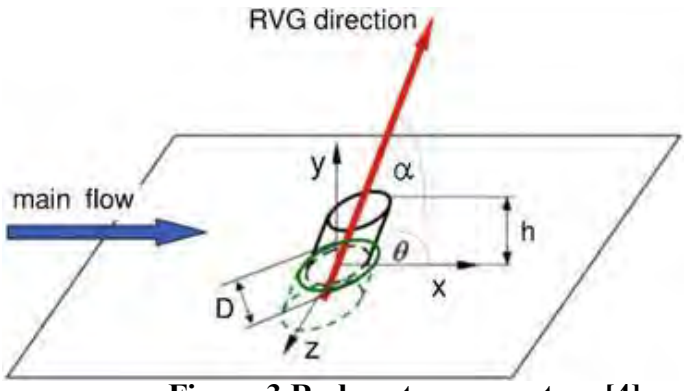

Figure 3 Rod vortex generators [4]

With the available aerodynamic investigation of RVGs and their promising influence in improvement of performance, the next technical analysis would be to investigate their influence on noise generation and transmission. This would give a complete technical framework for the application of RVGs in industries like turbo-machines, helicopters and wind turbines. In case of

wind turbines, the importance of an acoustic investigation is paramount. The results of this analysis will certainly influence the acceptance of the usage of wind energy by the general public.

Given the push for implementing renewable energy consumption into public life, several investigative campaigns into assessing the aero acoustics of wind turbines are available in literature. Investigations into understanding the fundamental flow physics involved in various flow regimes of a wind turbine is thoroughly analyzed by Bastankhah et al [9]. A thorough discussion on computational approaches, from estimating noise sources using mean flow and turbulence statistics to high fidelity unsteady approaches (DNS, LES) is available by Colonius T et al [10]. Information regarding discretization schemes and the effects of artificial dispersion and dissipation on uniform and non uniform grids is available in this report.

Targeting the dominant turbulent boundary layer trailing edge noise, various computational approaches have been demonstrated by Wouter in [11]. He studied both Navier-Stokes and Lattice Boltzmann methods to predict noise. Trailing edge noise is analyzed for an asymmetrically beveled 25° edge. The flow physics and the noise emissions around a teeth, combed teeth and straight edge configurations is studied to understand serrations. As a result of these studies, a shape optimization has been proposed which reduces the noise by approximately 2 dB.

An interesting investigation was conducted at JAXA, the Japanese Aerospace Exploration Agency, where the combination of two techniques – using protruding rounded lower edge PRLE for the lower side and VGs for the upper side of flaps to reduce air frame noise [12]. It is found that PRLE decreases noise generation by side vortices from the flap side edges and the upper vortices generated by VGs. They found a reduction of 1.5 dB(A) OASPL with only VGs and the combined technique reduced noise by around 4 dB(A). Computational investigations was conducted using LBM methods in the commercial package PowerFLOW from Exa. This was validated with experimental results.

Computational aero acoustics is the branch which deals with numerical methods for sound prediction. Direct methods like Direct numerical simulations (DNS) solves the compressible Navier-Stokes equations demanding high computing resources. The crux of CAA is the huge difference in the acoustic scales and the flow variables scales which makes it challenging to model a domain to account for both these extreme end scales in a single domain.

Hybrid approach simplifies this issue by first computing using a CFD solver and then implementing an acoustic analogy. This allows for both steady and transient simulations. Integral methods- Lighthill' analogy, Kirchoff's integral, FW-H method, Linearized Euler equations and spectral methods are some of the various acoustic models available.

Integral methods consists of solving the general solution for wave propagation in free space as an integral over all sources. Lighthill's analogy also known as the famous acoustic analogy is a different form of Navier-Stokes equation with wave operators and acoustic sources in the fluid

flow. Source term contains physical sources and sources describing the propagation in medium. The far field sound is computed as the volume integral over the source filled domain.

Many modifications have been introduced to this analogy to account for sound flow interaction effects and others. Ffowcs Williams and Hawking (FW-H) method modifies the Lighthill analogy to avoid a volume integral. With an assumption that the source region is limited, it is enclosed by a control surface (FW-H), it computes the surface integrals over monopole and dipole sources. For sources outside the FW-H surface, additional volume integral over quadrupole sources defined by Lighthill tensor.

Using this approach for bodies in arbitrary motion, Farassat eliminated the use of generalized functions and implemented boundary conditions on the moving blade directly for rotorcraft and propeller noise applications [13]. Implementing a useful form of this equation, Schmitz [14] analyzed the sources of noise and its mitigation techniques for helicopter blades. Harmonic noise radiation patters in hover and forward flight regimes is analyzed with noise radiation modeling to understand the origins of noise. High speed impulsive noise- extreme form of harmonic noise for a single rotor helicopter is investigated extensively for its relationship between the thickness noise and the tip Mach number. Both steady and unsteady rotor blade loading in investigated. Several methods to decrease this noise like lowering tip Mach numbers, blade plan-form changes with leading edge serrations, active on blade control of thickness noise and others have been tested with experimental data . Useful insights into various mitigation techniques is presented in this paper.

2.3.1. Methodology

For a preliminary study, linear noise theory is implemented to study thickness and loading noise. Since there exist experimental data-sets for the sound produced by the UH-1H helicopter model rotor in hover Boxwell [14]. it was used as one of the validation cases for the tool development. An in-house acoustic code is developed using Tecplot 360. Tecplot 360 is a visualization and analysis software with built-in macros for scripting and also provides python scripting options. Since it allows input of flow data in various formats, it is suitable for a general tool that can be used for CFD cases obtained from various commercial codes.

In order to study the various parameters of FW-H analogy, the simple Formulation 1 of Farassat is first implemented [15]. It is an integral solution to the FW-H analogy. It is expressed as

$$4\pi p(x,t) = 4\pi(p_T(x,t) + p_L(x,t)) = \\ = \frac{\partial}{\partial t}\int_{f=0}\left[\frac{\rho_0 v_n}{r\,(1-M_r)} + \frac{p\cos\theta}{cr\,(1-M_r)}\right]_{ret} dS + \int_{f=0}\left[\frac{p\cos\theta}{r^2\,(1-M_r)}\right]_{ret} dS \quad (1)$$

The grid for the model helicopter case and the pressure distribution is given as input. The helicopter rotor blade surface is discretized into small cells which act as acoustic sources. Here, the CFD mesh cells act as acoustic sources. Various parameters of the equation are calculated for each and every source cell. The normal velocity v_n is computed using the angle between the normal vector to the surface and the velocity vector obtained due to rotation. r is the distance between the observer and the source cell. M_r is the Mach number towards the observer. This value is found through the angle between the velocity vector and the radiation vector given by the vector joining the observer and the source panel. $cos\Theta$ is the local angle between the normal to the surface and the radiation vector. All these parameters are computed for every cell at the time of computation for each time step. Here, the time of computation is the source time (emission time) also called the retarded time τ. These values are then integrated over their respective source cell area at proper emission time. In Formulation 1, the terms are differentiated with respect to observer time (t). This is done numerically in the code. The observer time is obtained using the retarded time equation

$$g = \tau - t + \frac{|\, x - y(\eta, \tau)\,|}{c} = 0. \tag{2}$$

Due to the doppler shift, each source cell will have its own observer time at which it is detected depending on its distance from the observer. The steady pressure distribution for the loading term is supplied from CFD simulation. Initially the surface integration was obtained through a mid-point formula which is a second-order approximation. The differentiation scheme used for observer time derivatives was also second-order. Later fourth order differentiation scheme was also implemented. The blade surface, given as input is taken at time instant t=0 and it is rotated through azimuth increments to complete a given number of periods. At given observer time instant, all the source panels with the correct emission time, contributing to the noise signal are added to get the acoustic pressure pulse.

The analysis was conducted for 1/7-scale model of the UH-1H helicopter rotor in hover, having two rectangular blades with NACA0012 profile with radius of 1.045m, tip Mach number of 0.8 and with the observer located at a distance of 3R from the rotor axis in the rotor plane. The blades are untwisted and un-tapered with aspect ratio of~13.71 as shown in Figure 4. The pressure data is obtained from a separate CFD simulation. The computational model is described in more details in [16]. These simulations were conducted using a cell-centered, block-structured, parallel code SPARC with a Spalart--Allmaras turbulence model with a mesh of 3 million volumes. The acoustic signal obtained had to be flipped due to the reverse direction of probing of the acoustic parameters in the implemented Formulation 1. Various studies like the grid dependency, time step dependency, experimental input parameters were conducted using Formulation 1. This led to a reference case of 7028 surface cells and time step of 0.5°.

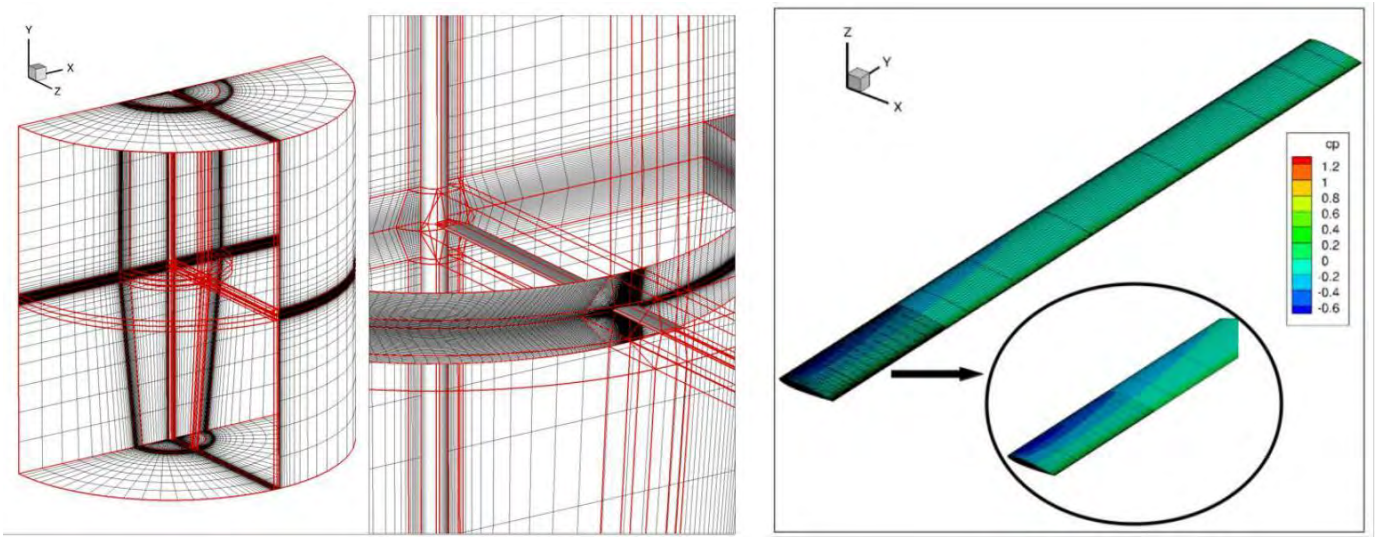

Figure 4 UH-1H model helicopter rotor a) grid topology with local refinement of $3*10^6$ volumes (7208 surface cells) (b) pressure coefficient (C_p) contour [16]

It is found that the peak negative amplitude of the acoustic pressure signal was under predicted compared to experimental values. Also, compact and non-compact body conditions are important in acoustics. For a non-rotating body, compactness condition necessitates that the size of the source body be much shorter than the acoustic wavelength. For rotating bodies it is dependent on observer time and position as demonstrated by Farassat [17]. Numerically, when the blade surface is divided into many small source cells, it is necessary that the compactness condition is satisfied by every single surface panel. It implies that for each source cell, the acoustic field should be related to the global parameters of the rotating body, for example the thickness noise to the net rate of mass injection, loading noise to the net force on the body. If the sources are non-compact instead of the net force contributing to the noise signal, only the local pressure would be accounted for. These compactness conditions also depend on the observer time and position making it quite challenging to numerically quantify them for each and every source cell and at each time interval. Furthermore, the observer time derivative in Formulation 1 increases computation time and decreases the accuracy of the results. Farassat developed Formulation 1A taking all of these aspects into account. 1A has observer time derivative converted into observer space derivative. This has led to many advantages such as development of moving observer and quadrupole noise formulations. The Formulation 1A as proposed by Farassat in [15] is of the form:

$$4\pi p_T(x,t) = \int_{f=0} \left[\frac{\rho_0 \dot{v}_n}{r\left(1-M_r\right)^2} + \frac{\rho_0 v_n \hat{r}_i \dot{M}_i}{r\left(1-M_r\right)^3} \right]_\tau dS + \int_{f=0} \left[\frac{\rho_0 c v_n \left(M_r - M^2\right)}{r^2\left(1-M_r\right)^3} \right]_\tau dS, \quad (3)$$

$$4\pi p_L(x,t) = \int_{f=0} \left[\frac{\dot{p}\cos\theta}{cr\left(1-M_r\right)^2} + \frac{\hat{r}_i \dot{M}_i p \cos\theta}{cr\left(1-M_r\right)^3} \right]_\tau dS + \int_{f=0} \left[\frac{p\left(\cos\theta - M_i n_i\right)}{r^2\left(1-M_r\right)^2} + \frac{\left(M_r - M^2\right) p\cos\theta}{r^2\left(1-M_r\right)^3} \right]_\tau dS.$$

p_T , p_L, v_n, M_i, M, p represent the thickness noise term, loading term, space derivative of normal velocity, space derivative of Mach number in unit direction, Mach number and space derivative of pressure respectively. In this formulation, the pressure signal is expressed as a sum of far-field and near-field terms. Near-field terms are of the order $1/r^2$ and far-field ones are of the order 1/r. The variables are differentiated with respect to source time (τ). The signals from both Formulations 1 and 1A are validated against the experiment.

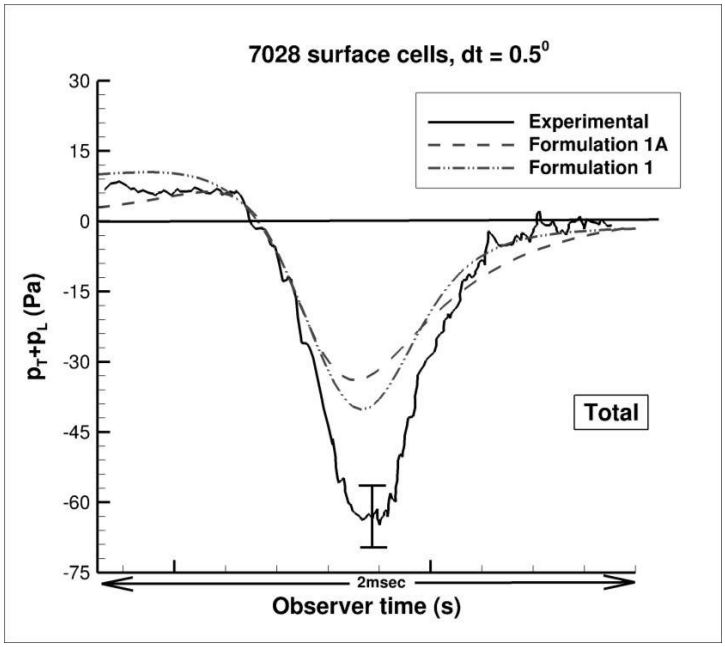

Figure 5 In-plane acoustic pressure signal recorded at 3R (MT = 0.8) from acoustic code and Boxwell [14]

The correct shape of the acoustic signal is captured very well by the developed acoustic tool. The numerical results under-predict the experimental values which point towards the limitations of the formulation itself and the assumptions of the linear theory. Formulation 1A under-predicts the peak amplitude even more than Formulation 1. However, Formulation 1A improves the

efficiency of the numerical algorithm and also reduces computation time by converting from time to space derivative. The surface integration is a critical step in the computation and since the errors present in this stage only get amplified with numerical differentiation, it is imperative to reduce these numerical errors. This forms the basis of future work to understand the reasons for under-prediction at moderate Mach number helicopter hover cases. Aside from this, the sensitivity of the surface raises the question of how precisely the blade has to be modeled when compared to the experimental blade. The geometrical twist of the blade might contribute in increasing the magnitude of the peak amplitude since the component of the in-plane noise is drag force. Experiment data predicts an uncertainty of +/- 10 Pa between twisted and un-twisted blades. Since the space derivatives (Formulation 1a) and time derivatives (Formulation 1) are present in the integral solution, the grid and time dependency studies are important to better understand the modeling of acoustic pressure signals. Also, there could be compressibility effects near the tip region for even high subsonic cases.

This tool provides flexibility in terms of studying the different types of noise terms individually, in terms of analyzing the individual parameters of the equation thus providing opportunities to implement noise control methods. Thickness, loading, near-field and far-field terms can be individually analyzed. Also enables to study noise contribution from different blade portions such as the leading edge, trailing edge and blade tips and at various observer locations aiding in better understanding of sound generation and propagation.

2.3.2. Present work

To validate the new aero-acoustic code developed, it is being implemented to study acoustic signal from elementary source such as a monopole. Using the model as in [18] the code is implemented for a pulsating sphere in harmonic motion.

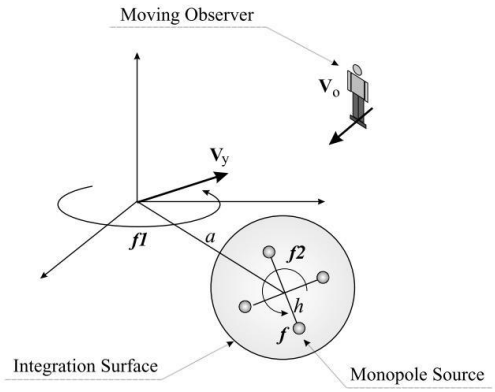

Figure 6 Surface modeling for a pulsating monopole

For investigating the noise generated by wind turbines, unsteady pressure data is needed from CFD simulations. To obtain this, currently unsteady simulations are being conducted for NREL Phase VI rotor blade in NUMECA software. The wind turbine blade has an S809 profile with 76 hexahedral blocks , mesh size of 8.8 million control volumes. Currently simulations are being conducted for inlet velocities = 7 and 10 m/s with SA and EARSM turbulence modeling.

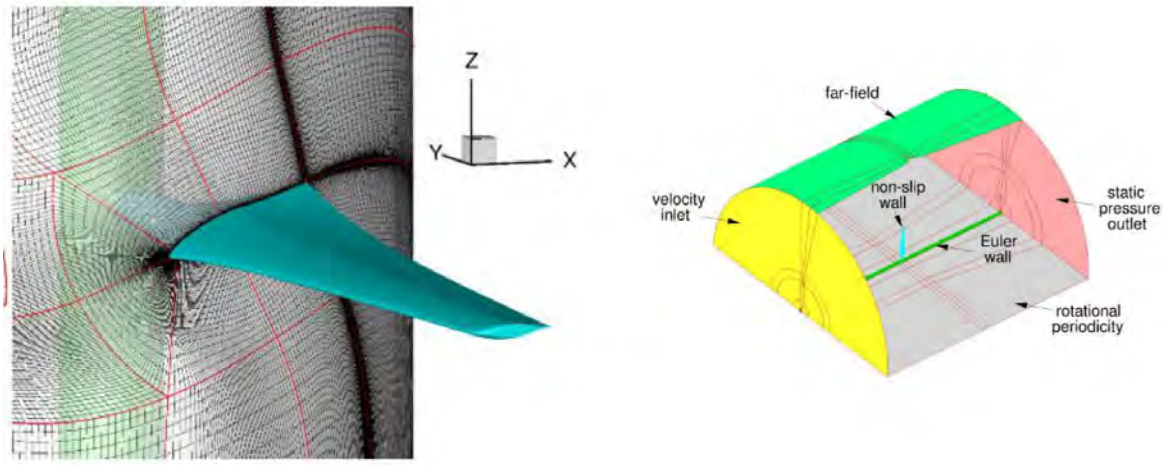

Figure 7 NREL Phase VI rotor – grid and computational domain

2.3.3. Outlook

- Acoustic code:

- To complete the validation of the code for all elementary sources, it will also be validated for a dipole source.
- To improve the under prediction of peak negative amplitude, quadrupole implementation will be considered.
- Another development is to also study porous surface implementation to take care of all the non linear terms generating sound.

- CFD simulations:

- To continue ongoing unsteady simulations for the NREL wind turbine blade without RVGs and then to conduct unsteady simulations for the same wind turbine blade with RVGs.
- To conduct LES simulation for S809 profile using OPENFOAM for both with and without RVGs.
- The pressure distribution from these CFD simulations will be given as input to the developed acoustic code to compare the sound generated with and without RVGs.
- Sound produced in these cases can also analyzed using the pressure field obtained from CFD simulations.

- Secondments:

- Early next year, to investigate using broadband noise tool BATMAN, developed by VKI (based on Amiet's theory) to explore the possibility of developing the BATMAN tool to investigate noise in flow separation cases. If successful, to then use the tool to investigate broadband noise generated by wind turbines both with and without RVGs.

2.3.4. References

[1] Design Criteria for and Applications of the Vortex Generator Mixing Principle, Taylor H. D, U. A. C. Report, M-15038- 1, February 1948.

[2] Schubauer GB, Spangenberg WG. Forced mixing in boundary layers, J Fluid Mech 1960;8:10–32

[3] Lin JC. Review of research on low-profile vortex generators to control boundary-layer separation. Prog Aerospace Sci 2002;38:389–420.

[4] Doerffer P, Flaszynski P and Szwaba R 2009 Polish Patent P. 389685.

[5] Doerffer P, Hirsh C, Dussauge J P, Babinsky H and Barakos G N 2010 Unsteady effect of shock wave induced separation. Notes on Numerical Fluid Mechanics and Multidisciplinary Design, Springer.

[6] Flaszyński P and Tejero Embuena F L 2013 RANS numerical simulation of effectiveness of vortex generators in a curved wall nozzle, IMP PAN Report No. 365/2013 (in polish).

[7] Fernando Tejero, Doerffer P and Szulc O, Shock wave induced flow separation control by air jet and rod vortex generators , IMP PAN, Task Quarterly: scientific bulletin of Academic Computer Centre in Gdansk, Vol 19, No 2, 167-180, 2015.

[8] Javier Martinez Suarez, Vortex generators application for reduction of boundary layer separation on wind turbine blades, IMP PAN, 2016.

[9] M. Bastankhah, and F. Porté-Age, Wind tunnel study of the wind turbine interaction with a boundary-layer flow: Upwind region, turbine performance, and wake region, Physics of fluids 2017.

[10] Tim Colonius , Sanjiva K. Leleb, Computational aeroacoustics: progress on nonlinear problems of sound generation, Science direct 2004.

[11] *Aeroacoustics Conference*, (June), 6–13. http://doi.org/10.2514/6.2017-4030.

[12] Farassat, F., “Linear Acoustic Formulas for Calculation of Rotating Blade Noise,” AIAA Journal, Vol. 19, (9), September 1981, pp. 1122–1130.

[13] Fredric H. Schmitz , The challenges and possibilities of a truly quiet helicopter, 29th Alexander A. Nikolsky Honorary lecture, Journal of the American Helicopter society 61, 041001 (2016).

[14] Boxwell D.A., Schmitz, F., and Yu, Y. (1978). Hovering Impulsive Noise : Some measured and calculated results. Nasa/Technical Memorandum 78N32831.

[15] Farassat, F. (2007). Derivation of Formulations 1 and 1A of Farassat. Nasa/Technical Memorandum- 214853, 214853(March):1–25.

[16] Szulc, O., Doerffer, P., and Tejero, F. (2016). Passive control of rotorcraft high-speed impulsive noise. Journal of Physics: Conference Series, 760(1).

[17] Farassat, F. (1975). Theory of Noise Generation From Moving Bodies With an Application to Helicopter Rotors. Technical report.

[18] Casalino D.(2003), An advanced time approach for acoustic analogy predictions, Journal of sound and Vibration, 261 (4) 583-612

2.4. ESR-7: Aerodynamic Noise Reduction by Porous Materials

Turbofans remain the primary choice of propulsion for modern airliners. Nonetheless, the noise they produce is still a major annoyance for bystanders, especially those who live close to airports. Hence, the regulation on aviation noise limit is becoming more stringent, and it is of practical interests for the industry to introduce novel means of noise reduction [1]. Various promising solutions have been proposed in the literature, such as leading edge serrations [2]. However, many of these studies were performed using very simplified models, which may not always represent the real situations [3]. Hence, the objectives of the project undertaken by the ESR-7 are as follow: 1) To propose a scaled model that improves existing one for emulating the noise generated by a fan stage, 2) To apply novel noise mitigation technique to the model and extend the knowledge for potential industrial applications.

2.4.1. The rod-linear cascade for emulating rotor-stator interaction mechanism

One of the relevant noise generation mechanisms in a turbofan is the rotor-stator interaction mechanism [1]. This refers to the periodic impingement of turbulent wake from a rotating blade (i.e., rotor) onto a downstream stationary blade (i.e., stator). The process can be observed in both the fan-outlet guide vane (OGV) stage (i.e., bypass flow system) as well as the compressor/turbine stages (i.e., core flow system). Nonetheless, as turbofan designs are trending toward higher bypass ratio, so does the noise contribution of the fan stage [4]. Thus, it is of practical interests to gain insights on the aeroacoustics of the noise generation mechanism and to explore potential noise mitigation strategies. However, performing full investigation on a complex system, such as a complete fan stage, may become quite challenging and expensive, especially in early stages of design (e.g., prototyping). Instead, it would be more accessible to first examine models based on simplified geometrical elements that still preserve the flow features of interest, such as the rod-airfoil configuration [5].

The rod-airfoil configuration (hereon abbreviated as RAC) has been quoted to be suitable for emulating the rotor-stator interaction mechanism due to the quasi-tonal and broadband excitation induced by the rod wake onto the airfoil. However, there are various features inherent of the rotor-stator aeroacoustics which are absent in the RAC due to the usage of the isolated, symmetrical airfoil; two of which will be addressed here. Firstly, typical stator vanes in a fan stage are designed with large camber, installed at high incidence angle, and arranged in a cascade to achieve significant flow deflection. Secondly, the high-solidity environment typical of a fan stage results in noticeable acoustic interactions between one blade and its neighbours. Collectively, these aerodynamics and aeroacoustics implications are often referred to as the *cascade effects* [6].

Consequently, replacing the isolated airfoil of the RAC with a linear cascade is beneficial to obtain a more representative setup for emulating the fan wake-OGV impingement mechanism, hence the rod-linear cascade model (hereon referred to as RLC). The RLC in present study, however, only considers one blade to undergo rod wake impingement for several reasons: 1) it is difficult, if not impossible, to control the shedding phase of multiple rods and 2) to avoid unwanted feedback mechanism due to the presence of multiple vortex streets [7]. To this scope, recent activities have been focused on designing the RLC and characterizing its aerodynamics

and aeroacoustics characteristics. The study is performed using a numerical scheme based on Lattice-Boltzmann Method (LBM) with the intent to reproduce the RLC setup as closely as possible to an experimental setting, and to obtain a comprehensive description of the flow field and the acoustics response of the model. Moreover, the outlook of this study is to employ the RLC for studying the effects of various noise mitigation techniques in a turbomachinery-like flow field, including potential impacts on the aerodynamic performance.

The numerical study considers an experimental setup as shown in Figure 8, which consists of a contraction and a test section where the RLC model is installed. The contraction has been designed to achieve freestream velocity of 75 m/s, which is slightly lower than typical fan stage flow field at "approach" condition. Meanwhile, the cascade profile is derived from the NASA-Glenn Source Diagnostics Test (SDT) fan stage [8], which is a lab-scale turbofan model. Consequently, the rod diameter is 5.2 mm such that the Karman vortex street is turbulent with fundamental shedding frequency that equals to the first BPF (i.e., blade passing frequency) of the SDT. A segment of the test section upstream of the RLC is curved to compensate for the flow deflection produced by the cascade.

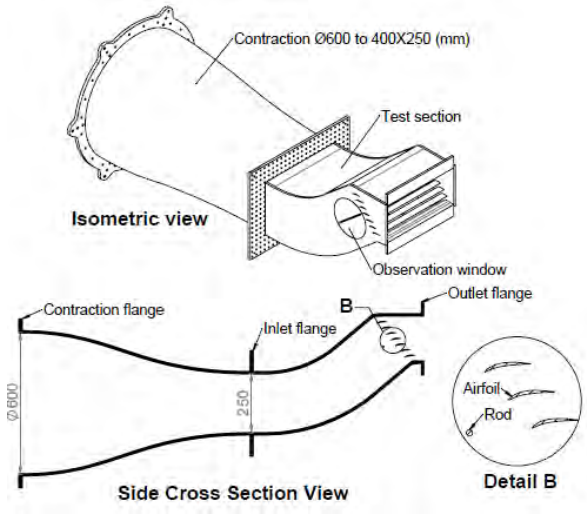

Figure 8: Technical drawing of the rod-linear cascade model

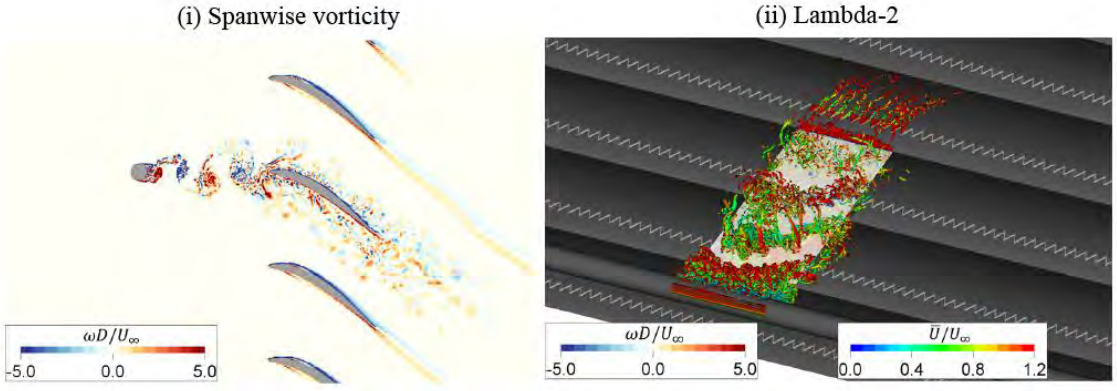

Figure 9: (i) Spanwise vorticity contour and (ii) lambda-2 visualization surrounding the RLC

Figure 9 presents flow field visualization surrounding the RLC model. The rod is shown to produce turbulent Karman vortex street, which impinges on the central blade of the cascade. Figure 9 (i) illustrates an instance when one of the large vortices is deformed and broken into smaller structures by the central blade leading edge. Moreover, due to its turbulent nature, the rod wake loses its spanwise correlation as it is convected toward the central blade, as shown in Figure 9 (ii).

In order to measure the sound produced by the RLC, the permeable surface formulation of Ffowcs-Williams & Hawking acoustics analogy (FW-H) has been employed [9]. The permeable surface is designed to enclose the exterior of the test section. Subsequently, the acoustic waves coming from the test section are sampled on this surface at a rate of 56 kHz for 56 ms (i.e., 160 vortex shedding cycles). The FW-H analogies are then computed on microphones located outside of the test section. The microphones are arranged in an arc located at the midspan of the test section. The arc radius is 1 m with the origin located at the rod center. The arc's zero angle reference is aligned with the streamwise direction at the test section outlet. The microphones are located on the arc with the range of [-150º, 150º] and 10º increment.

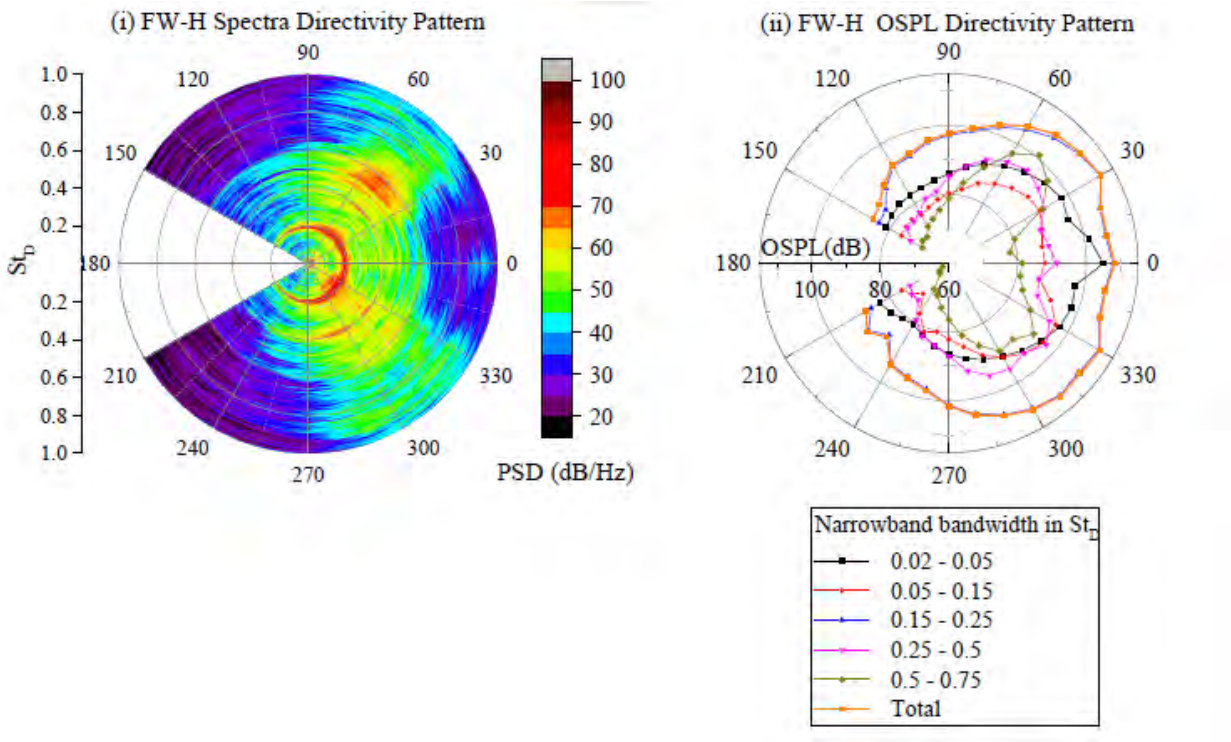

Figure 10: Far-field sound directivity pattern in terms of, (i) power spectral density and (ii) overall sound pressure level

The results of the FW-H computations are shown in Figure 10. The power spectral density (PSD) in Figure 10 (i) is estimated using the Welch's method with Hanning windowing and 50% FFT bin overlap. The PSD is then normalized into logarithmic scale with reference pressure of 20

μPa, while the frequency is expressed as Strouhal number based on the rod diameter. Meanwhile, Figure 10 (ii) shows the integration of the PSD at various frequency ranges, and subsequently expressed as overall sound pressure level (OSPL). To illustrate the acoustics field surrounding the RLC, the dilatation field and the RMS of pressure fluctuations contours are provided in Figure 11.

The acoustic response of the RLC model is characterized by the presence of several tones at the fundamental shedding frequency and its harmonics, as well as a broadband base. The narrowband corresponding to the fundamental frequency is also shown to be dominating all of the observed directions. The sound of this narrowband is observed to be due to the large scale structures in the rod wake impinging on the central blade. The sound waves are then diffracted by the adjacent blade and guided into the inter-blade channels, before travelling further downstream towards the outlet. This process is quite different from the RAC, in which the sound produced by the airfoil is radiated to the far-field without being obstructed, resulting in dipole-like directivity pattern. The acoustic-blade interaction in the RLC also causes strong pressure fluctuation regions inside the inter-blade channels, somewhat similar to the Parker's resonance in turbomachinery [10]. Nonetheless, at higher frequency ranges where the sound wavelength is smaller than the chord length of the cascade blade, the acoustic diffraction becomes less efficient. As a result, the pressure fluctuation inside the inter-blade channel at the high frequency ranges is relatively weaker and concentrated surrounding the central blade.

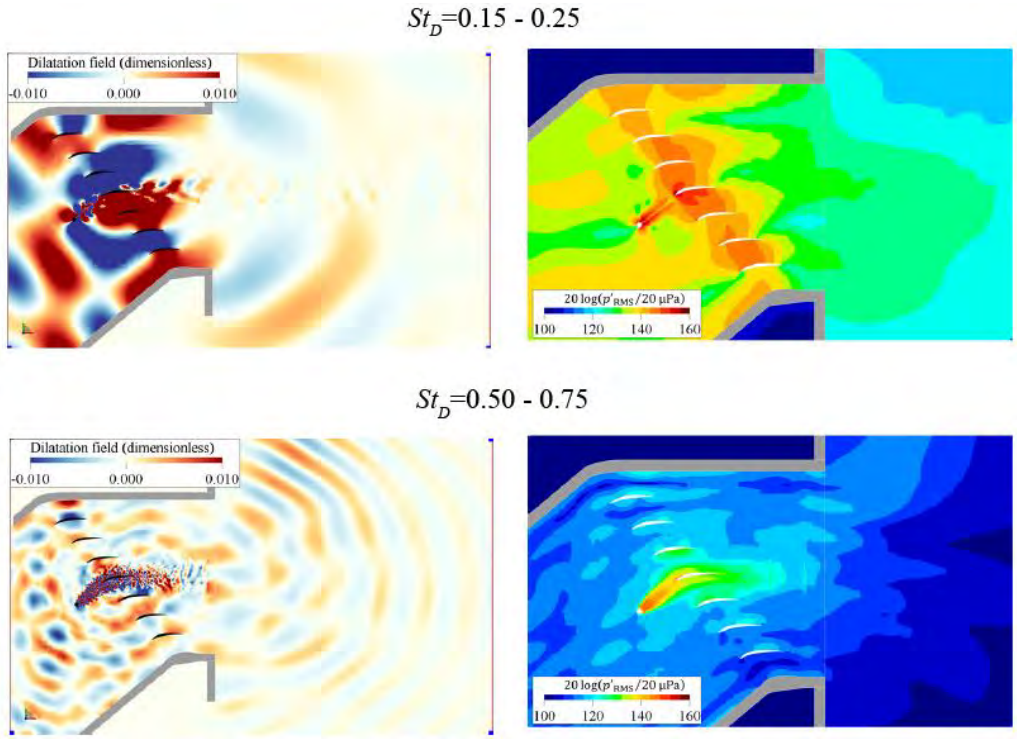

Figure 11: Bandpass-filtered contour of instantaneous dilatation field (left) and RMS of pressure fluctuations (right) for Strouhal ranges of 0.15 – 0.25 and 0.5 – 0.75

From the aerodynamics perspective, the linear cascade shows similarities in the loading characteristics as the OGV of the SDT, as shown in Figure 11 (a). The discrepancy at the

downstream half of the blade is likely due to the different stagger angle being used. Although the rod wake has minor effect on the mean loading characteristics of the central blade, Figure 11 (b) shows high level of surface pressure fluctuation surrounding the leading edge. The adjacent blades, however, register significantly lower level, implying that the aerodynamic excitation due to the rod wake is limited to the central blade.

To conclude, the RLC couples two aeroacoustics phenomena, namely the leading edge noise generation by interaction with oncoming turbulence, and the acoustics-blade interactions due to the usage of high solidity cascade. Since these phenomena are inherent in fan wake-OGV interaction mechanism, the RLC presents the opportunity as a test rig for exploring novel noise mitigation techniques for such applications. It is conjectured that noise reduction within the RLC could be achieved with the following mechanisms: 1) dampening the surface pressure fluctuation at the central blade leading edge, 2) enhancing decorrelation or phase interference effects of the leading edge sources, and 3) reducing the cascade effects with acoustic treatment on the blade surface. Future studies would also allow elucidating the impact of various noise mitigation strategies on the OGV performance since the geometrical details are preserved.

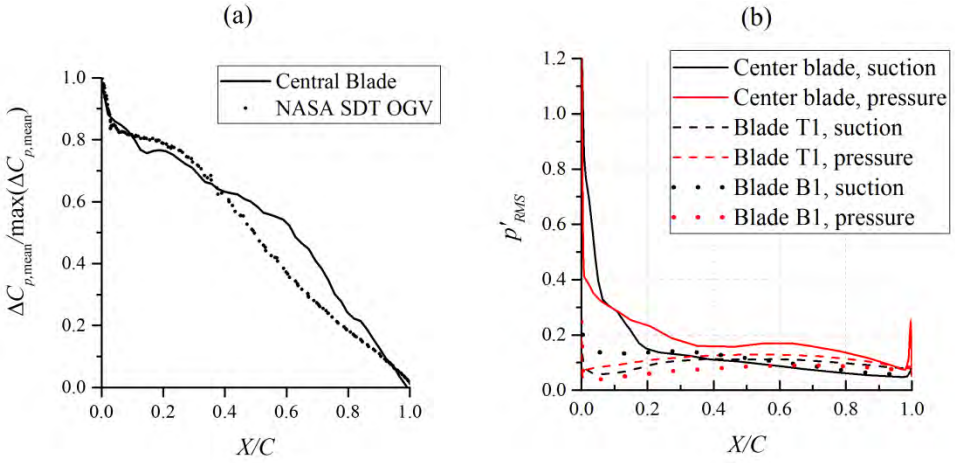

Figure 12: (a) Normalized mean surface pressure difference between pressure and suction side of the central blade, and (b) RMS of surface pressure fluctuation on the cascade blades

2.4.2. Validation study of PowerFLOW's porous media model

Noise reduction with porous material has gained significant interest lately, with applications for various engineering purposes are proposed regularly [11], including for airfoil self-noise [12]. More recently, Rubio-Carpio et al. have applied metal-foam trailing edge on a NACA 0018, and found that its noise was reduced at low to mid frequency ranges [13]. The authors concluded that the noise reduction mechanism is very likely due to the unsteady transpiration across the porous material, since non-permeable porous trailing edge did not result in noise reduction. However, due to the limitations of the experimental technique, they were not able to observe the flow field in proximity of the porous material surface. To this scope, numerical simulations can be used to complement the information obtained from the experiments. Nonetheless, this will require accurate numerical representation of the physical properties of porous material.

Empirical models for describing flow through porous material have been developed for the past few centuries. In various literature, it is agreed upon that the porous material causes pressure loss on the permeating flow. One of the widely used model, the Hazen-Dupuit-Darcy (HDD) [13], is able to describe the physical phenomena that contribute toward the momentum losses inside the porous material. The Hazen-Dupuit-Darcy model essentially shows that a flow through a porous material of a certain thickness would experience pressure loss (ΔP). Moreover, the model characterizes the porous material with two parameters, namely the permeability (K) and the form coefficient(C). The HDD model is expressed mathematically as follows.

$$\frac{\Delta P}{h} = \frac{\mu}{K} v_d + \rho C v_d^2$$

where ρ is the fluid density, μ is the dynamic viscosity, $v_d = Q/A$ is the Darcian velocity, Q is the volumetric flow rate, A the cross-section area of the sample, and h is the material thickness.

The two terms on the right side of the HDD model describe two mechanisms that cause the pressure loss. The first term, which is linear with the Darcian velocity, refers to the loss due to viscous drag. Meanwhile, the second term is related to the inertial loss (e.g., due to flow acceleration) and it becomes important for high Reynolds number flow through the porous material. Both physical mechanisms are considered in the porous material (PM) model of PowerFLOW.

To validate the PM model used in PowerFLOW, simulations are performed on a porous material characterization test rig. The porous material that will be used is based on a NiCrAl metal-foam manufactured by *Alantum*. The manufacturer specified the metal-foam characteristics with mean cell diameter d_c. Empirical characterization of the porous material has been performed by Rubio-Carpio et al. [13] using the test rig depicted in Figure 13. The porous material parameters are summarized in Table 2.

It is also important to note that PowerFLOW uses slightly different nomenclature to describe the HDD parameters, namely the viscous resistivity ($R_V = \mu/K$) and inertial resistivity ($R_I = C$). Furthermore, there are two different models of porous media in PowerFLOW – APM (acoustics porous medium) and PM (porous medium). While both describes the porous material as an equivalent fluid region governed by the HDD model, the APM also considers acoustic absorption property of the material. Additionally, APM is assigned with a porosity (Φ) value which would affect the flow behavior at the interface in between the regular fluid region and the APM region.

Table 2 Parameters for characterizing transport phenomena in the metal-foam samples

d_c (μm)	Φ (%)	R_V (Ns/m^4)	R_I (m^{-1})
450	89.28	29850	9758
800	91.65	6728	2613

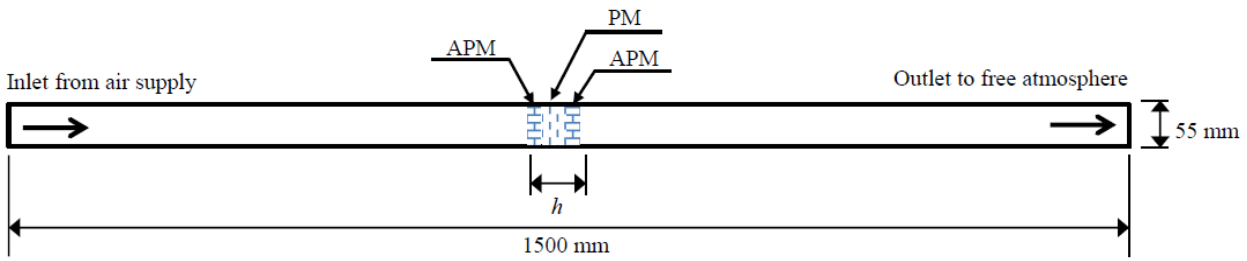

Figure 13: Simplified sketch of the test rig for characterizing the permeability and the form coefficient of the metal-foam sample

In present study, the test rig in Figure 13 has been replicated in PowerFLOW, with the tube inlet replaced by a mass flow inlet, while atmospheric pressure is defined at the tube outlet. The metal-foam sample is modeled as 3-layer of acoustics porous material (APM) - porous material (PM) - APM, in order to consider the flow interaction at the surface of the metal-foam. The APM region accounts for 20% of h (i.e., $0.1h$ thick on both ends of the sample) and the rest of the thickness is prescribed as PM region. Meanwhile, mass flow rate boundary condition, corresponding to certain Darcian velocity (v_d), is assigned to one end of the tube, and freestream pressure p_∞ at the other end. The wall of the tube is prescribed with no-slip boundary condition.

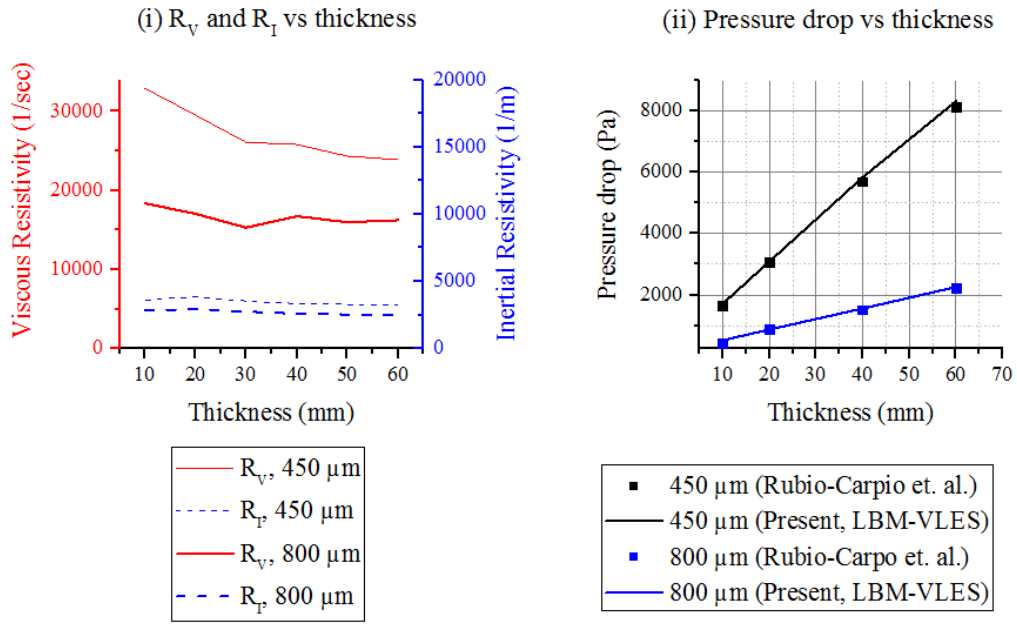

Figure 14: Resistivity value and pressure drop variation with metal-foam sample thickness in the test rig

The variation of viscous resistivity R_V , inertial resistivity, R_I, and the pressure drop trend in the porous material characterization test rig is shown in Figure 13. The resistivity values were extracted from measurements of Rubio-Carpio et al. [13], which is then provided into the APM and PM models in PowerFLOW. The Darcian velocity v_d – 2.35 m/s (450 µm) and 2.55 m/s (800 µm) remains constant for the respective samples depending on the pore size. In Figure 13 (i), the R_V shows more variation compared to R_I as the sample thickness decreases, which was similarly

observed by Dukhan and Minjeur [14]. Furthermore, in Figure 13 (ii), the APM-PM combination used in the numerical study also results in good agreement for various tested sample thickness.

The pressure and flow velocity distribution within the test rig is shown in Figure 14. The streamwise location has been normalized by sample thickness (h), the pressure as $(p - p_\infty)/\Delta p$, and velocity as u/v_d. As expected, pressure drop only takes place inside the APM-PM region, which is also consistent for all of the samples, regardless of thickness or porosity (i.e., pore size). Similarly, velocity increases linearly across the APM-PM region and eventually becomes constant further downstream to maintain constant mass flow rate within the tube. Based on these results, PowerFLOW APM-PM models are considered to be reliable for emulating the one-dimensional transport phenomena within the porous material.

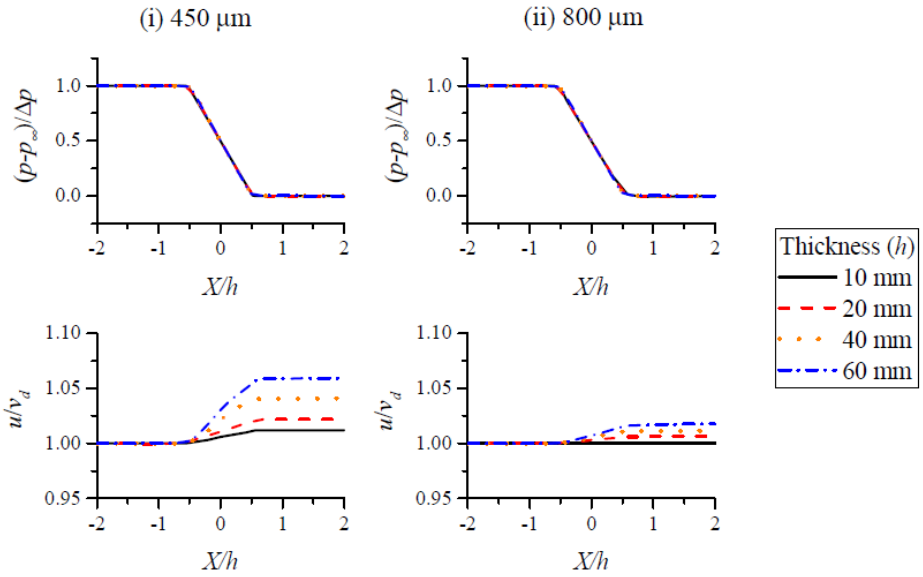

Figure 15: Streamwise sample of pressure and flow velocity at the center of the test rig

2.4.3. Preliminary Conclusion and Outlook

The project undertaken by ESR-7 is focused on the application of porous material for reducing rotor-stator interaction nosie in turbofan. The groundwork for this project has been laid in this report with two subjects: 1) the rod-linear cascade model and 2) validation of porous material model in PowerFLOW. To conclude, the RLC is a system that couples two aeroacoustics phenomena, namely the leading edge noise generation by interaction with oncoming turbulence, and the acoustics-blade interactions due to the usage of high solidity cascade. Since these phenomena are inherent in fan wake-OGV interaction mechanism, the RLC presents the opportunity as a test rig for exploring novel noise mitigation techniques for such applications. It is conjectured that noise reduction within the RLC could be achieved with the following mechanisms: 1) dampening the surface pressure fluctuation at the central blade leading edge, 2) enhancing decorrelation or phase interference effects of the leading edge sources, and 3)

reducing the cascade effects with acoustic treatment on the blade surface. Future studies would also allow elucidating the impact of various noise mitigation strategies on the OGV performance since the geometrical details are preserved.

Validation studies on the porous material also result in good agreement against the experiments. Nonetheless, more validation studies will be performed on more realistic cases, such as the trailing edge noise case of Rubio-Carpio et al. [13]. Afterward, the PM model will be applied to the RLC and its performance will be compared with other promising noise mitigation techniques, such as leading edge serrations. Some interesting concepts, such as a combined porous-serrated leading edge, may be introduced to obtain even greater noise reduction.

2.4.4. References

[1] Groeneweg, J. F., & Rice, E. J. Aircraft turbofan noise. *Journal of turbomachinery*, Vol.109, No. 1, 130-141, 1987.

[2] Chaitanya, P., Joseph, P., Narayanan, S., Vanderwel, C., Turner, J., Kim, J. W., & Ganapathisubramani, B. "Performance and mechanism of sinusoidal leading edge serrations for the reduction of turbulence–aerofoil interaction noise." *Journal of Fluid Mechanics*, Vol. 818, 435-464, 2017.

[3] Casalino, D., Avallone, F., Gonzalez-Martino I., and Ragni, D., "Aeroacoustics Study of a Wavy Stator Leading Edge in a Realistic Fan/OGV Stage", *Intl. Symp. On Transport Phenomena and Dynamics of Rotating Machinery*, Maui, HI, December 2017.

[4] Casalino, D., Hazir, A., & Mann, A., "Turbofan broadband noise prediction using the Lattice Boltzmann Method". *22nd AIAA/CEAS Aeroacoustics Conference*, 2945, 2016.

[5] Jacob, M. C., Boudet, J., Casalino, D., and Michard., M., "A Rod-Airfoil Experiment as Benchmark for Broadband Noise Modeling." *Theoret. Comput. Fluid Dynamics*, Vol. 19, 171–196, 2005.

[6] Finez, A., Jacob, M., Jondeau, E., & Roger, M., "Experimental investigation of trailing-edge noise from a linear cascade of cambered airfoils." In *17th AIAA/CEAS Aeroacoustics Conference (32nd AIAA Aeroacoustics Conference),* p. 2876, 2011.

[7] Kumar, S. R., Sharma, A., & Agrawal, A., "Simulation of flow around a row of square cylinders." *Journal of Fluid Mechanics*, Vol. 606, 369-397, 2018.

[8] Woodward, R., Hughes, C., Jeracki, R., & Miller, C., "Fan Noise Source Diagnostic Test--Far-field Acoustic Results." In *8th AIAA/CEAS Aeroacoustics Conference & Exhibit* (p. 2427), 2002.

[9] Williams, J. F., & Hawkings, D. L. "Sound generation by turbulence and surfaces in arbitrary motion." *Philosophical Transactions of the Royal Society of London A: Mathematical, Physical and Engineering Sciences*, Vol. 264, No.1151, 321-342, 1969.

[10] Parker, R., “Resonance effects in wake shedding from parallel plates: some experimental observations.” *Journal of Sound and Vibration*, Vol. 4, No. 1, 62-72, 1966.

[11] Roger, M., Schram, C., & De Santana, L., “Reduction of airfoil turbulence-impingement noise by means of leading-edge serrations and/or porous material.” *19th AIAA/CEAS aeroacoustics conference*, p. 2108, 2013.

[12] Geyer, T., Sarradj, E., & Fritzsche, C., “Measurement of the noise generation at the trailing edge of porous airfoils.” *Experiments in Fluids*, Vol. 48, No. 2, 291-308, 2010

[13] Carpio, A. R., Martínez, R. M., Avallone, F., Ragni, D., Snellen, M., and Van Der Zwaag, S., “Broadband Trailing Edge Noise Reduction Using Permeable Metal Foams.” In *46 th International Congress and Exposition of Noise Control Engineering*, p. 27-30, August 2017.

[14] Dukhan, N., & Minjeur, C., ”Minimum Thickness for Open-Cell Metal Foam to Behave as a Porous Medium.” *40th Fluid Dynamics Conference and Exhibit*, p. 4618, 2010.

2.5. ESR 8/15: Novel experimental diagnostics for the reduction of turbulence-body interaction noise

ESR8 (TUD) is investigating a novel implementation of Tomographic-Particle Image Velocimetry (Tomo-PIV) for elucidating the noise reduction mechanism of trailing edge serrations. Tomo-PIV allows velocity field information to be extracted from an experiment without the need of intrusive equipment. Recent developments in Tomo-PIV systems have enabled larger measurement volume with the use of HFSB (Helium Filled Soap Bubbles); this system is subsequently referred to as large-scale Tomo-PIV.

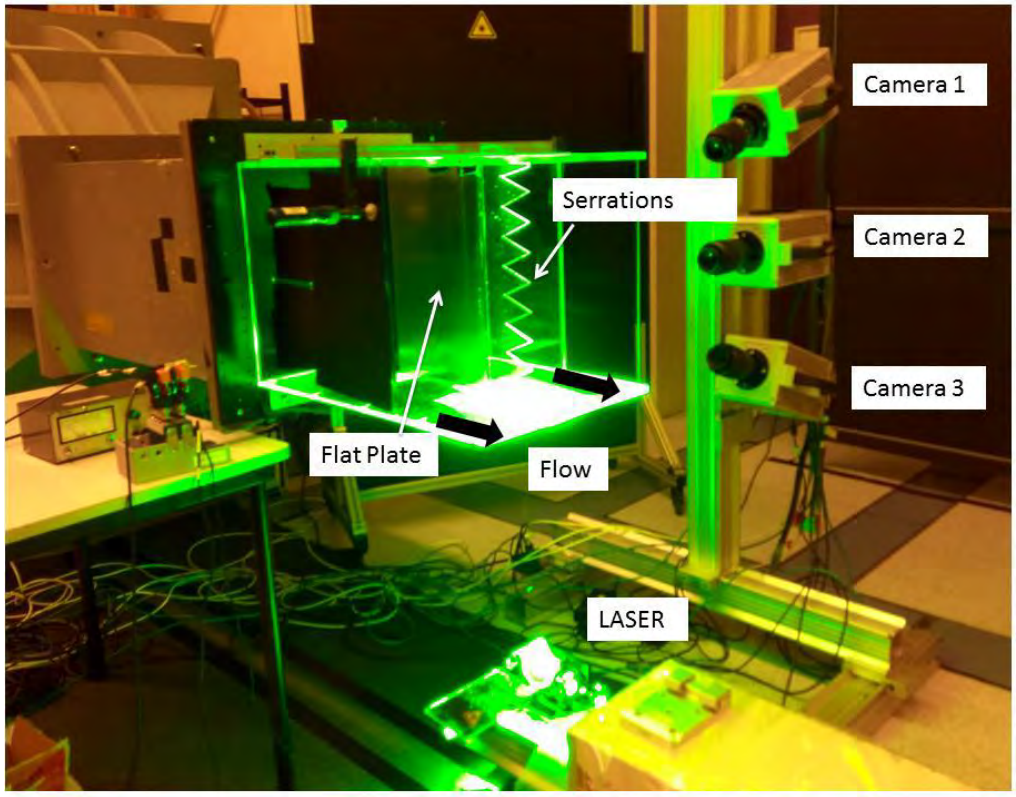

Figure 16 Experimental setup for 3D-PTV using HFSB

Present effort has been focused into studying the flow structure surrounding a trailing edge serration using the large-scale Tomo-PIV. Furthermore, pressure reconstruction scheme can be applied onto the PIV velocity map to quantify surface pressure fluctuation on the serration, which is related to the far-field sound characteristics. A preliminary study is performed using a flat plate whose trailing edge can be equipped with serrations (Figure 16). Experimental results have shown that Tomo-PIV is able to produce accurate boundary layer quantities as shown in Figure 17. Furthermore, the surface pressure fluctuations obtained with the Tomo-PIV will also be compared against those from surface-mounted microphones. Future study will be focused on understanding how the modification of serration geometries affect the local flow field and consequently, far-field noise.

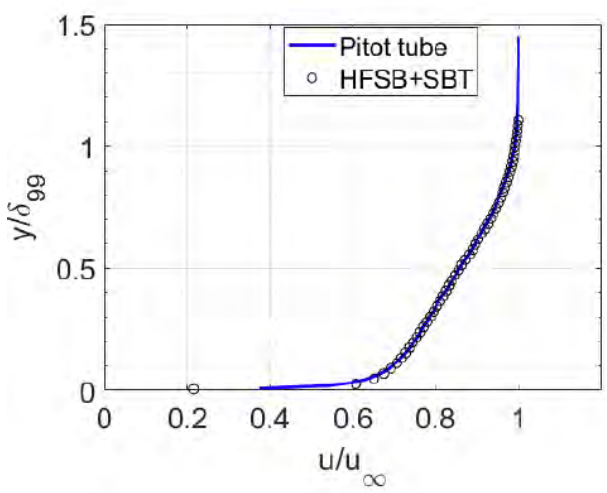

Figure 17 Mean boundary layer profile comparison from pitot tube and tomo-PTV

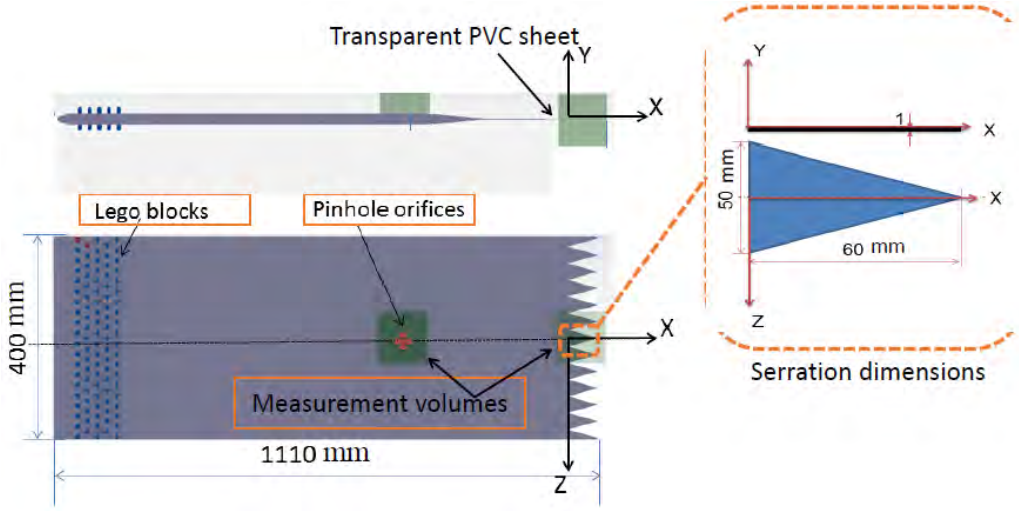

Figure 18 Details of serrated flat plate for the experiment

2.6. ESR 9: Fan proximity acoustic treatments for improved noise suppression in turbofan engines

The growth in air traffic increases the levels of noise in the population, which require the implementation of new technologies to accomplish the noise regulations in Europe, United States and worldwide. The aircraft noise generated during take-off and landing is key for the certification of aircrafts, the engine noise being dominant at take-off and the airframe noise when landing.

The turbofan engine, used in most commercial aircraft, represents a large contributor to the overall aircraft noise, which must be reduced in order to achieve any improvement in the overall aircraft noise reduction. Fan noise is one of the dominant engine sources both at approach and at take-off, resulting in a critical noise-reduction target for the next generation of turbofan engines [1].

The next generation of turbofan engines will have higher bypass ratios (BPR), hence a significant increase in fan diameter (D) but without an increase in liner length (L) to minimize nacelle weight. Consequently, as the performance of the liners is proportional to L/D, the larger diameter nacelles will result in higher noise levels. In order to recover the liner performance, every effort is needed to apply liners to other available duct areas. An area that has not been fully evaluated or exploited in the past is the duct casing in the immediate proximity of the fan rotor. The so-called Fan Proximity Liners (FPL) consists of the fan case, the Over-The-Rotor (OTR) region and the interstage, see Figure 19(a). A Foam Metal Liner (FML) installed in the Williams International FJ44-3A engine is shown in Figure 19(b).

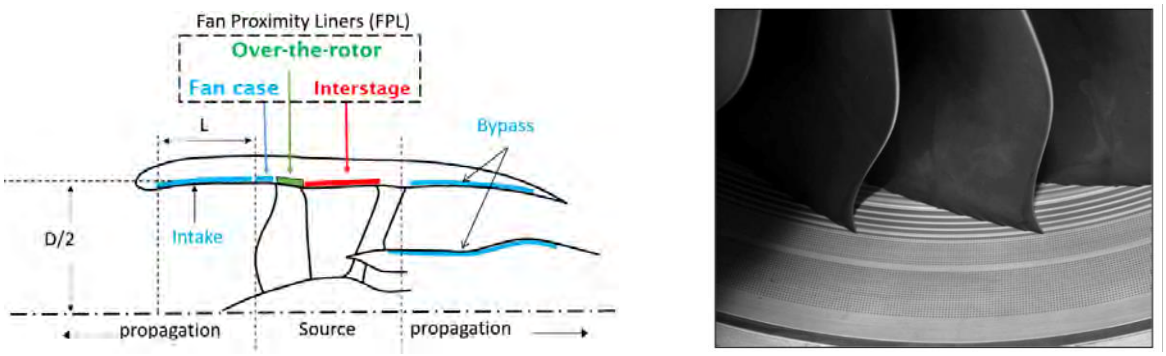

(a) **(b)**

Figure 19 (a)Standard liners (Intake and Bypass) and Fan Proximity Liners (FPL) and (b) Foam Metal Liner (FML) installed in the Williams International FJ44-3A engine [2]**.**

The OTR region presents a harsh aeroacoustic environment which limits the materials and technologies that can be used for the design of the liners. These conditions define a series of characteristics that would be required for the materials, including high acoustic absorption, high-temperature resistance, containment properties/high impact resistance, low flammability and minimal fluid retention [2,3,4].

Over-The-Rotor acoustic treatments have been investigated during the last decade as a technology with the potential to further attenuate the fan noise in turbofan engines, mainly at

NASA GRC, where significant noise reductions have been measured. The tests showed a range of noise attenuation and loss in aerodynamic performance (measured as loss in adiabatic efficiency), which rely upon the liner design used, the test rig and the operating conditions. Details of the experimental set-up and discussion of the results are available in the literature, but a summary of the results obtained is shown in Table 3.

Table 3 Summary of OTR published experimental results.

Publication	***Noise Attenuation***	***Loss in Adiabatic Efficiency***
Sutliff et al. [5]	4 dB PWL (inlet & aft)	-
Elliot et al. [6]	1 dB OAPWL	-
Sutliff et al. [7][2]	5 dB inlet PWL / 2.5 dB OAPWL	1-2 %
Hughes and Gazzaniga [8]	-	6.5 – 9.8 %
Bozak et al. [9]	-	0.75 %
Gazella et al. [10]	1 dB / 3 dB (inlet/aft) PWL	-
Bozak and Dougherty [11]	2.5-3.5 dB (inlet) PWL	-

The authors of the published experimental work suggest that OTR liners mitigate the acoustic near-field, showing that noise attenuation of this acoustic treatment is caused by a combination of acoustic attenuation, source modification (acting as a pressure-release surface) [3,2] and attenuation of the rotor-stator noise [2]. However, a consensus on the physical mechanism for the noise attenuation using OTR acoustic treatments has not been reached [2].

The lack of full understanding and consensus on the physical mechanism of noise attenuation using OTR acoustic treatments and the need for a prediction method to estimate the optimum surface impedance for OTR liners has been identified in the literature [2]–[4], [7]. Accordingly, the objectives of this project are:

(1) Improve the understanding of the acoustic attenuation of fan proximity liners, OTR liners in particular, through the development of theoretical models, numerical simulations and experimental validation.
(2) Use the acquired understanding to develop a prediction method to guide the choice of low-TRL fan proximity liner designs for optimal noise reduction whilst meeting installation constraints for application to commercial turbofans.

The modelling of OTR liners is a challenge due to the high complexity of the physics involved. The sound generation, propagation and attenuation in the vicinity of the fan are each a complex problem on their own right. The sources of sound are a combination of tones of the blade passing frequency and aerodynamic broadband sources that can be divided into self-noise (trailing edge noise and tip clearance noise) and interaction noise (fan-OGV interaction and tip-BL interaction). The suggested modification of the sources by the liner and the expected high-pressure fluctuations acting on the liner surface make the modelling of the propagation and attenuation non-trivial, involving non-locally reacting cavities and non-linear effects. If the tip relative Mach number is supersonic, shock waves would be present adjacent to the liner increasing the difficulties of impedance prediction.

The approach taken thus far in the project has been mainly analytical, aimed at developing models that simplify the complex physics, yet being representative of the *acoustic* problem. The analytical models will be cross-verified with selected numerical simulation results obtained with LMS Virtual.Lab and will be validated experimentally against published NASA results and data from experiments planned at ECL. A brief summary of each of these approaches is presented below.

2.6.1. Current activity

- **Analyical approach**

The problem is simplified to a cylindrical semi-infinite lined duct matched with a semi-infinite hard wall duct. The noise source(s) are placed within the lined section at an axial distance from the hard-lined interface representative of the space available for a real OTR liner in a commercial turbofan engine. A system of static monopoles and/or dipoles have been implemented so far, and it is planned to extend the current formulation to rotating sources. A diagram of the simplified problem is show in Figure 20.

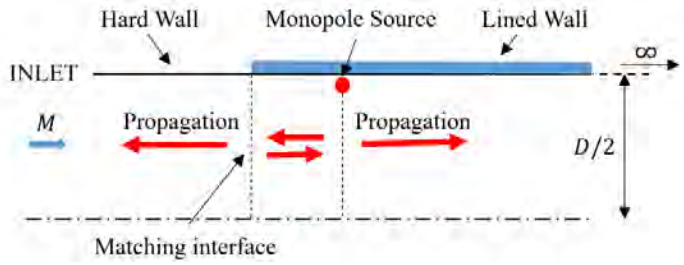

Figure 20 Diagram of the semi-infinite hard-lined duct.

The pressure field generated by the source system can be obtained by adapting the Green's function for a lined circular duct containing uniform mean flow[12] to the source model used and solving the matching problem at the interface between the lined and hard regions. This model allows to modify the radial and axial position of the source(s) to define the tip clearance and lined surface available respectively and then compute the axial power radiated into the upstream hard wall section to assess the performance of the liner.

Different impedance models are being used to define the acoustic impedance in the lined duct: (1) a constant impedance, which is useful to obtain the optimum values at specific frequencies, (2) SDOF/DDOF locally reacting liners, widely used in aeronautics, (3) acoustically treated circumferential grooves, which have been used in the NASA experimental tests. Established models are available for locally reacting SDOF/DDOF cavity liners but a new analytical model has had to be developed and verified to predict the behaviour of hard and acoustically treated annular grooves.

- **Numerical approach**

Training in the use of LMS Virtual.Lab has been received during a secondment to SISW, along with numerical simulations aimed at verifying the analytical models developed thus far in the project. The two main objectives of the simulations were:

(1) Provide high-fidelity reference solutions to cross-verify with the analytical propagation models, which include an infinite lined duct and a finite lined duct within an infinite hard wall duct, in both cases excited by a single static monopole point source and with uniform mean flow.
(2) Improve the understanding of the acoustic response of acoustically treated non-locally reacting grooves and provide a reference solution to cross-verify with the analytical impedance model developed for this kind of acoustic treatment.

- **Experimental approach**
  - The latest OTR experimental data published by R.F. Bozak and R.P. Dougherty [11] will be used to validate the analytical results, for which a reliable model of the acoustically treated grooves is required.
  - A validation test is being planned for a two-month secondment at Ecole Centrale de Lyon (ECL) (Lyon, France). The aim of the experiments will be to assess the performance of an acoustic liner in terms of reducing the tip noise radiated from (a) the flow over the airfoil at and near the tip and (b) the flow through the gap between the tip of an airfoil and a flat surface. The surface will be tested with no liner and with a liner insert flush mounted in the flat surface.

2.6.2. Preliminary conclusion and outlook

It has been shown that the power generated by a monopole source in a duct depends on the impedance boundary condition, the source excitation frequency and radial position. This dependence can lead to a negative liner insertion loss (IL), i.e. an amplification for some parameter combinations such as a liner impedance with a low resistance and positive reactance. Further work, including numerical FEM simulations, is being developed to understand this and to determine whether this could occur with real fan source distributions.

The analytical predictions have shown that a point monopole source located at a realistic position relative to an OTR liner, could provide a broadband power insertion loss (IL) of around 4 dB, with significant attenuation over a wide range of source excitation frequencies.

Results have been obtained for a dipole point source oriented normal to the chord of a staggered fan blade and hence directed at a certain angle relative to the duct axis, using a model for the effective impedance of acoustically treated circumferential groove. These have been compared with the published experimental data, indicating that the source model is able to reproduce the measured asymmetry between co-rotating and counter-rotating spinning modes. However, understandably, it cannot predict the significant noise amplification effects attributed to an

aerodynamic interaction of the blade tip with the grooves [11]. The predicted acoustic power attenuation or insertion loss is found to be within the same range as the experimental results, i.e. 2.5 - 3.5 dB (PWL).

Preliminary comparisons of the numerical simulations of the full geometry of acoustically treated grooves and the results obtained with the analytical impedance model show a satisfactory agreement. This confirms that the acoustic response of the grooves is well captured in the liner propagation models developed thus far.

The analytical propagation model will be extended to a finite length liner, within an infinite hard wall duct, to better represent the OTR liner performance in practice. Future modelling work includes a compact ring of point sources, distributed rotating sources and a simple model of the mean flow between the rotor blades. In addition, it is planned to predict the azimuthal and PWL spectra of the different experimental OTR configurations and to compare those with published NASA data.

Details of the analytical formulation, the verification cases and the validation of the models will be published in due course and are out of the scope of this interim report.

2.6.3. References

[1] D. L. Huff, "Technologies for Turbofan Noise Reduction," *10 th AIAACEAS Aeroacoustics Conf.*, no. September, pp. 1--27, 2004.

[2] D. L. Sutliff, M. G. Jones, and T. C. Hartley, "High-Speed Turbofan Noise Reduction Using Foam-Metal Liner Over-the-Rotor," *J. Aircr.*, vol. 50, no. 5, pp. 1491–1503, 2013.

[3] M. Jones, T. Parrott, D. Sutliff, and C. Hughes, "Assessment of Soft Vane and Metal Foam Engine Noise Reduction Concepts," *15th AIAA/CEAS Aeroacoustics Conf. (30th AIAA Aeroacoustics Conf.*, no. May, pp. 11–13, 2009.

[4] M. G. Jones and B. M. Howerton, "Evaluation of Novel Liner Concepts for Fan and Airframe Noise Reduction," *22nd AIAA/CEAS Aeroacoustics Conf.*, pp. 1–18, 2016.

[5] D. L. Sutliff and M. G. Jones, "Low-Speed Fan Noise Attenuation from a Foam-Metal Liner," *J. Aircr.*, vol. 46, no. 4, pp. 1381–1394, 2009.

[6] D. Elliott, R. Woodward, and G. Podboy, "Acoustic Performance of Novel Fan Noise Reduction Technologies for a High Bypass Model Turbofan at Simulated Flight Conditions," *15th AIAA/CEAS Aeroacoustics Conf. (30th AIAA Aeroacoustics Conf.*, no. May, pp. 11–13, 2009.

[7] D. L. Sutliff, D. M. Elliott, M. G. Jones, and T. C. Hartley, "Attenuation of FJ44 turbofan engine noise with a foam-metal liner installed over-the-rotor," *AIAA Pap.*, vol. 3141, no. May, p. 2009, 2009.

[8] C. E. Hughes and J. A. Gazzaniga, "Effect of Two Advanced Noise Reduction Technologies on the Aerodynamic Performance of an Ultra High Bypass Ratio Fan," *15th AIAA/CEAS Aeroacoustics Conf. (30th AIAA Aeroacoustics Conf.*, no. May, pp. 11–13,

2009.

[9] R. Bozak, C. Hughes, and J. Buckley, “GT2013-95114,” in *The Aerodynamic Performance of an Over-The-Rotor Liner with Circumferential Grovees on a High Bypass Ratio Turbofan Rotor*, 2016, pp. 1–8.

[10] M. R. Gazella, T. Takakura, D. L. Sutliff, R. Bozak, and B. J. Tester, “Evaluating the Acoustic Benefits of Over-the-Rotor Acoustic Treatments Installed on the Advanced Noise Control Fan,” *AIAA/CEAS Aeroacoustics Conf.*, no. 23RD, 2017.

[11] R. Bozak and R. P. Dougherty, “Measurement of Noise Reduction from Acoustic Casing Treatments Installed Over a Subscale High Bypass Ratio Turbofan Rotor,” *2018 AIAA/CEAS Aeroacoustics Conf.*, pp. 1–14, 2018.

[12] S. W. Rienstra and B. J. Tester, “An analytic Green’s function for a lined circular duct containing uniform mean flow,” *J. Sound Vib.*, vol. 317, no. 3–5, pp. 994–1016, 2008.

2.7. ESR 11: Reduction of broadband aerodynamic noise of airfoils by geometrical and structural modifications

Turbulent flows interacting with solid surfaces are efficient sources of broadband noise. The turbulence-impingement noise of an airfoil placed in a highly disturbed flow is therefore considered a generic problem of primary engineering and research interest. Numerous applications are found in domestic, automotive and industrial environments, such as low-speed fans in engine cooling units or in ventilation systems, wind turbines and rotating-blade technology for aeronautical transport. Typically, a protection grid or a heat exchanger upsteam of a cooling fan, the rotor wakes of the fan of a turbofan engine impinging on outlet guide vanes or just atmospheric turbulence are sources of broadband noise for rotating blades or stationary vanes that cannot be directly controlled because they are inherent to the installation in the environment. Therefore alternative sound-reduction strategies must be sought in modifications of the blades or vanes that remain compatible with the aerodynamic performances. In recent years several studies have been done on the reduction of the turbulence-impingement noise mechanism by modifying the material and mainly the geometry of the leading edge [1][2][3]. Leading edge serrations, recently including random shape modifications, have been assessed, giving encouraging noise reductions [4]. Porosity applied on airfoils is another promising way of reducing the turbulent-impingement noise (TIN) but few extensive studies exist till now [2][5].

The current report presents the effect of sinusoidal leading-edge serrations and the effect of porosity of some airfoil parts. It constitutes continuation of a preliminary study in which both technologies have been compared[5], with promising results in terms of noise reduction even with non-optimized implementation. The point of interest is to provide an insightful view of the physical mechanisms of scattering vorticity into sound at the leading edge. In the case of a serrated edge the noise reduction mechanism originates from a destructive interference between the tips and roots of the serrations and from the rapid de-correlation of surface pressure fluctuations along the leading edge as the serration amplitude increases [6][7]. The action of porosity is presumably dealing with the effect of compressibility, in the sense that the impinging vortices are not blocked by the solid surface; part of the incident velocity slows down progressively, decreasing the inertia time variations by penetrating the permeable surface [2][5]. Of course, the feasibility of both techniques is strongly related to the main airfoil geometrical parameters that are the chord and the thickness. Advanced structures and geometries are presented in the following sections addressing each mechanism separately by different experimental techniques. This report summarize these techniques and deliver preliminary results which extent previous studies by the authors[2][5][8] providing an enlarged overview by investigating the three-dimensionality of TIN radiation.

2.7.1. Experimental campaign

The aforementioned noise reduction devices have been tested, performing various measurement techniques such as far-field acoustic measurements, time-resolved particle image velocimetry, noise localization (beamforming method) and acoustic impedance measurements on a complex-structure. Current results confirmed the acoustic efficiency of the serrated and porous airfoil

devices. Complementary studies are presently developed in parallel, such as the analytical modeling of turbulence-impingement noise. This will be achieved for the baseline airfoils by using three-dimensional Amiet's model and for the serrated airfoils by the analytical formulation recently derived by Ayton & Kim [9].Compared predicted and measured reduction spectra will be presented in the coming deliverables, together with a discussion about the possible deterioration of the aerodynamic performances.

All acoustic measurements were conducted in the low-speed anechoic open-jet wind tunnel of Ecole Centrale de Lyon (ECL). A rectangular nozzle with a vertical outlet cross-section of 15cm x 30cm delivers a uniform flow into the chamber with a speed ranging from 19 m/s to 32 m/s. In all tested configurations the turbulent flow is generated by a grid placed upstream of the nozzle contraction (cross-section 30 cm x 30 cm). The turbulent intensity and the integral length scale have been found of 4,5% and 9 mm, respectively, after fitting of a model von Kármán spectrum. All tested airfoils were held between two narrow supports that minimize sound reflection or masking and allow for far-field measurements in a wide range of oblique directions off the mid-span plane. A vertical microphone array installed on a rotating arc is used to measure the three-dimensional radiating pattern of TIN at a distance of 1.2 m from the airfoil leading-edge center point. A detailed description of the set-up and instrumentation has been done by Bampanis et al. [8].

- **Flat-plate airfoils**

Part of the work is aimed at producing a data base for TIN including the three-dimensionality of the radiated sound in combination with the effect of serrations. For this, a baseline airfoil and serrated versions are needed. In order that the data base can be used for the validation of analytical models, a thin-airfoil design has been chosen, starting from flat plates. Two flat-plate airfoils with wavy leading edges and one with a straight leading edge as baseline have been manufactured with a three-dimensional printer. The parameters of the two serrated versions are *a priori* tuned to the integral length scale ‘Λ’ of the incident turbulence, here measured as 9 mm, according to the observation by Chaitanya et al. [1] that efficient noise reduction depends on proper inclination angle and amplitude of the sinusoidal serrations. The three flat plates and the narrow-support installation are shown in Figure 21 (a) and (b).

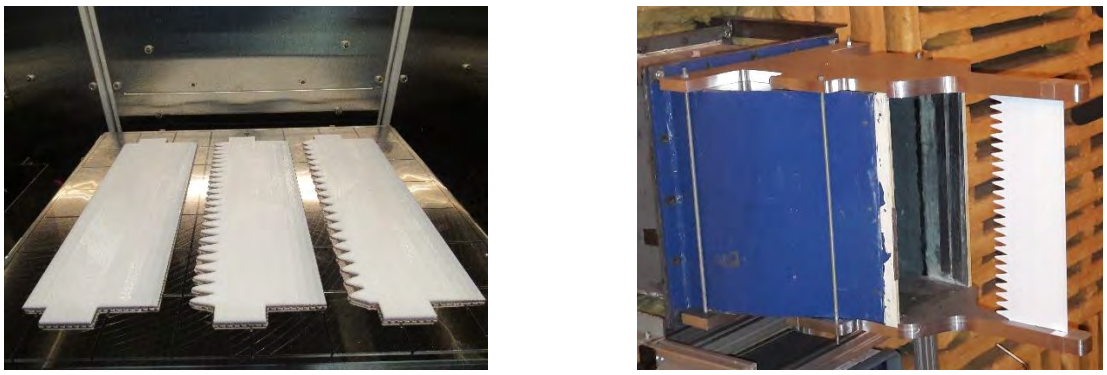

(a) **(b)**

Figure 21. Detailed pictures of the set-up and tested flat-plate airfoils (a) Flat plates: baseline, big serrations and small serrations (b) Nozzle with the narrow support plates

- **Porous airfoils**

Two different mock-up versions with inner porosity have been manufactured for the investigation of turbulence-porosity interaction noise (TPIN). The structural design of these mock-ups is motivated by both aerodynamic and acoustic considerations. The only difference between these versions is the extension of the central rigid plate of the frame at the leading edge. A wire-mesh metal cloth of $0.21\ mm$ thickness and porosity 40 is finally wrapped around the airfoil Figure 22. The metal cloth is aimed at allowing the partial penetration of the unsteady flow that is required to reduce the compressibility effect and at ensuring a minimum roughness for the external wetted surface. The inner porosity can have several beneficial acoustic effects.

Figure 22. Overview of porous-airfoil skeleton with recessed edge

Quantifying the actual contributions of these mechanisms on the overall performance is a challenging task that will be addressed in the coming months, apart from the direct interest of the expected reduction of turbulence-impingement noise at the leading edge.

- **Thick serrated airfoils**

A serrated NACA-0012 airfoil and the corresponding baseline airfoil have also been manufactured with the 3D printer, again with the chord of $100\ mm$ and the span of $300\ mm$. The aim was to allow for complete comparisons between the two tested reduction means. Indeed on the one hand the effect of airfoil thickness on serration-induced noise reduction can be assessed; on the other hand the performances of serrations and porosity can be compared on the same airfoil design. The leading-edge wavy pattern is the same as for the flat plates. A simple

geometrical formula also described by Paruchuri et al. [1] gives the three-dimensional design of the serrated NACA-0012 airfoil. A criterion of manufacturing a serrated leading-edge is to merge the serration root with the main body smoothly, preventing geometrical irregularities of the surface. The latter is 100 mm and the maximum chord length from serration tip to trailing edge is 110 mm. Choosing a constant mean chord for all mockups ensures that, as far as possible, they have same lift force linked to the total airfoil lifting surface at arbitrary angle of attack.

2.7.2. Results

- **Differences of far-field spectra**

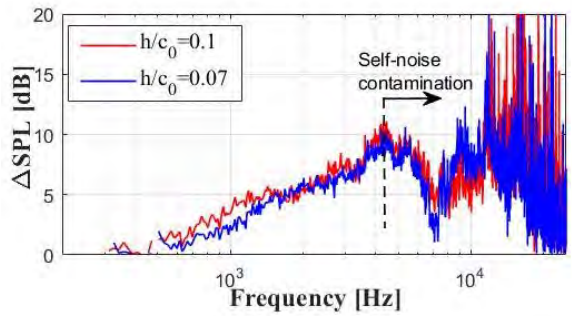

(a)

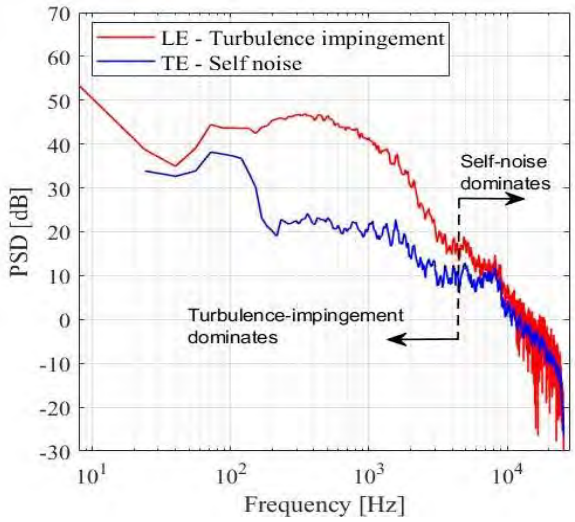

(b)

In the case of leading-edge serrations the reduction was found an increasing function of frequency up to a maximum of about 8-10 dB in the range 4-6 kHz. At higher frequencies a dramatic drop of the reduction was found, followed by another range of efficient reduction Figure 23(a). Separate measurements of airfoil self-noise have been made by removing the turbulence grid and forcing transition into turbulence in the boundary layers by tripping when needed. This self-noise is essentially trailing-edge noise and takes over TIN for frequencies typically beyond 4.3 kHz in Figure 23(b). This makes simple spectra subtraction inappropriate to evaluate the TIN reduction operating at the leading-edge. Similar results have been obtained with the porous airfoils but with reduction maxima substantially shifted in frequency, as reported in Figure 24(a). The serrated leading edge has shown better performance in low-mid frequencies, which was also observed by Roger et al. [1][5] for chord-based Strouhal numbers below 10.

Figure 23. (a): Noise-reduction spectra obtained for the serrated flat-plate airfoils by simple spectra subtraction (a) and typical far-field noise spectra comparing TIN and trailing-edge noise (b) for jet velocity, U_0 = 32m/s and observation angle, 90°, at the mid-span plane.

The same Strouhal number of 10 was observed in the aforementioned studies as the threshold beyond which the self-noise starts dominating. The reduction at high frequencies appears to be larger than for the serrations. However it must be noted that this is attributed partly to the reduction of trailing-edge noise also achieved by the porous treatment. Indeed the latter has an

action on the developing boundary layers and absorbing properties that reduce trailing-edge noise generation and radiation. Furthermore a larger reduction with a maximum of about 8 dB was obtained with the version 2 of the porous airfoil, thus with the recessed edge that allows putting continuous porosity in a small volume around the leading-edge, whereas the version 1 had maximum noise reduction of 6 dB Figure 24(b). This indicates that the leading edge of the airfoil is critical for an efficient action on the compressibility effect.

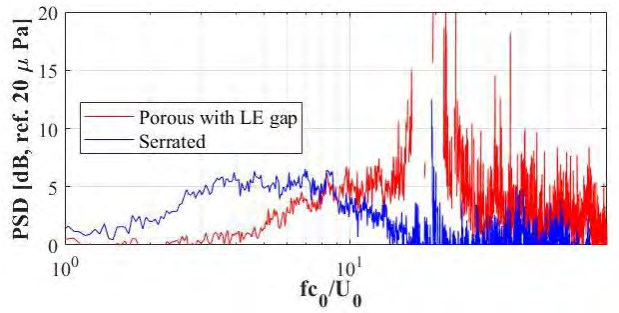

(a)

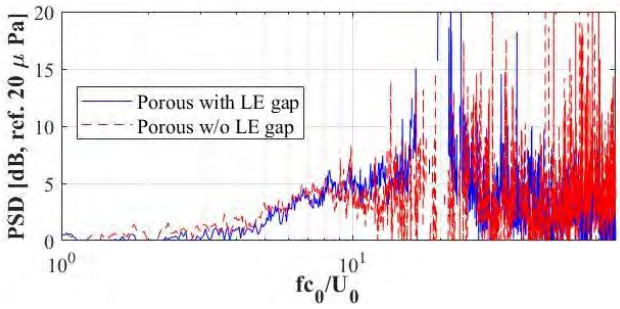

(b)

Figure 24. Compared noise-reduction spectra of porous and serrated airfoils in the mid-span plane at 90° (a) and compared reductions achieved with the versions 1 (red) and 2 (blue) of the porous NACA-0012 airfoil (b) for jet velocity, U_0 = 32m/s.

- **Source localization and extraction**

Advanced post-processing techniques of microphone arrays that extend the capabilities of conventional beamforming can be used to extract and quantify the acoustic signature of one source from a total sound field in which several sources contribute. Here the deconvolution algorithm called CIRA operated by LMS software has been used. A detailed description of the method is given by Piet et al. [10]. The whole setup and preliminary results have been described in detail by the authors [8]. Typical maps shown in Figure 25 correspond to the frequency range 4-4.5 kHz for the baseline and serrated flat-plate airfoils with h/c_0=0.1 where the far-field noise reductions start decreasing. Integrating the two selected areas at the leading and trailing edges (black rectangular boxes in Figure 25 (b), the contribution of each source defined as its integrated power is extracted, keeping in mind that the needed assumption of uncorrelated equivalent monopoles is believed a reasonable interpretation. The results are shown in Figure 26. The black curve is the logarithmic sum of the two sources including also part of the background noise. Indeed, at the frequency of 3.5 kHz the reconstructed TE noise starts to increase till the

frequency of 8 kHz. The reconstructed LE noise seems to decrease motononicaly from the low frequency of 1 kHz till the highest frequencies. It is worth noting that below 3 kHz the separation of the LE and TE areas is abusive in view of the resolution capabilities of the algorithm.

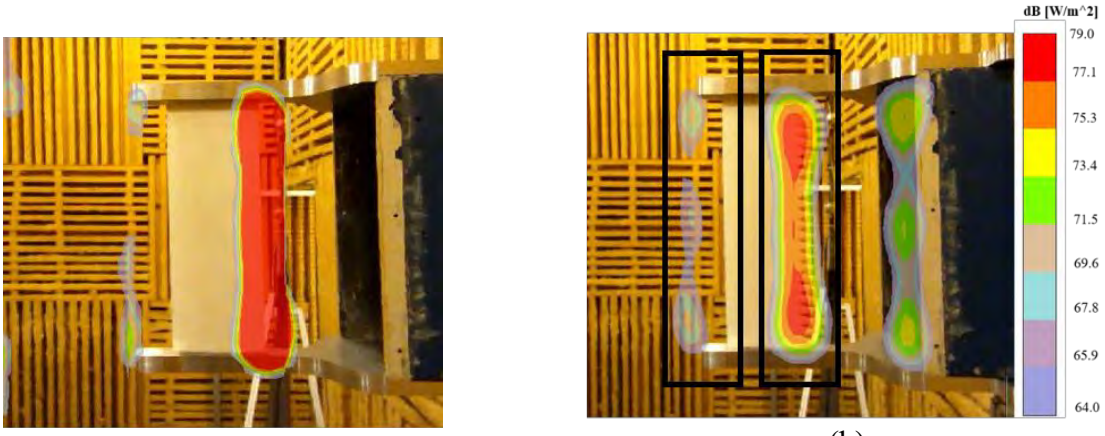

(a) (b)

Figure 25. Source-power color maps for the range 4-4.5 kHz measured with the baseline (a) and serrated flat-plate (b) airfoils. Flow from right to left.

Therefore the alternative estimate of the effect of serrations based on differences of the integrated source-power maps is believed to make sense only at higher frequencies. It leads to the results in Figure 26 (b), showing that the TIN reduction remains an increasing function of frequency up to the investigated high-frequency limit, with a maximum of more than 14 dB.

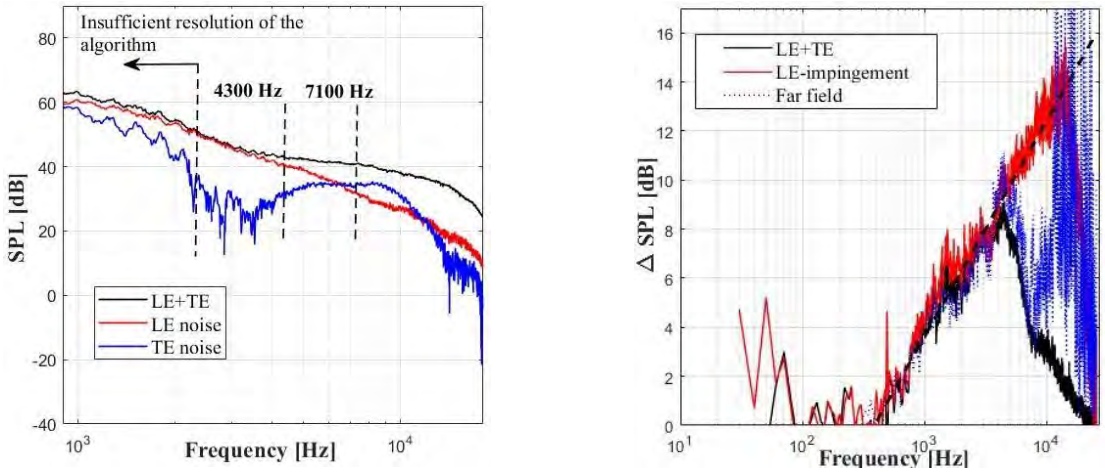

(a) (b)

Figure 26. (a): LE noise and TE noise extractions generated by the filtered array processing. (b): Noise reduction.

- **Particle image velocimetry measurements**

The three-dimensional features of the turbulence at the leading-edge will be obtained with a time-resolved tomographic particle image velocimetry (PIV) technique, both for a serrated flat-plate and NACA-0012 airfoil and for the corresponding baselines at a zero angle of attack. The three velocity components and their time history were recorded in a rectangular fluid volume. The measurements have be carried out in the open-jet low-speed W-tunnel of Delft University of Technology. Four different cases have been tested performing time-resolved tomographic and stereoscopic PIV. A metal grid made of flat rods was placed downstream of the nozzle contraction, generating nearly isotropic and homogeneous turbulence. The mean flow velocity ranges between 19-25 m/s measured with a pitot tube and validated by the PIV recordings after the velocity field reconstruction. All the mock-ups have the same mean chord of 100 mm and the same serration geometrical parameters.

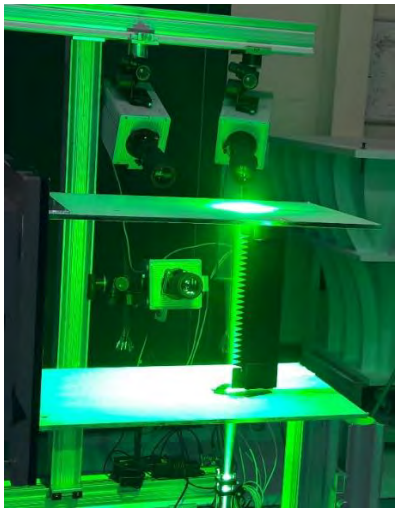

Figure 27. First set-up, serrated flat plate is held vertically

Two different tomographic PIV configurations were considered so as to access to different volumes at the position of the leading edge serrations, as it is presented in Figure 8. The origin of the Cartesian coordinate system for each configuration is selected at the position of the mean chord at the mid-span plane of each model. The first time-resolved tomographic PIV set-up is shown in Figure 27. The LaVision *DaVis 8.4* software was used for data acquisition. A description of the instrumentation, the principles and the process are given by Avallone [11][12].

Figure 28. Tomographic PIV measurement volumes: (a) First set-up, vertical held serrated flat plate (b) Second set-up, horizontal held serrated flat plate.

Preliminary results of the instantaneous, average velocity and vorticity of the flow have been obtained after the post-processing procedure. The average flow velocity in different sections extracted from the measured volume is shown in Figure 29.

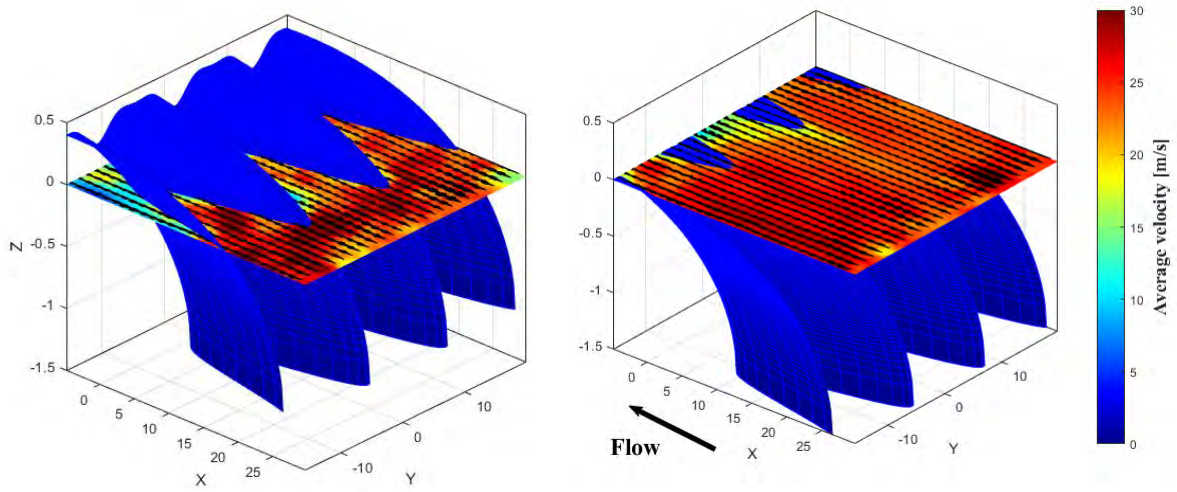

Figure 29. Preliminary results of the average velocity distribution in planar sections along the serrations height.

2.7.3. Conclusions

The present report has confirmed previous investigations of the turbulence-impingement noise reduction by means of either serrations or inclusion of porosity, for both flat-plate airfoils and the reference NACA-0012 airfoil. Apart from basic methods based on differences of far-field sound spectra a more refined approach based on microphone-array measurements has been shown to be more reliable at high frequencies for which turbulence-impingement noise is overwhelmed by trailing-edge noise. This allows to unambiguously demonstrate reductions of about 14-15 dB with the serrations that could not be observed from the basic far-field investigation. The performances of porosity seem to be less promising at the present state of knowledge but they are still under investigation.

2.7.4. References

[1] Paruchuri C, Subramanian N, Joseph P, Vanderwel C, Kim JW, Ganapathisubramani B. Broadband noise reduction through leading edge serrations on realistic aerofoils. *21st AIAA/CEAS Aeroacoustics Conf.* 2015;(June):1-29. doi:10.2514/6.2015-2202

[2] Roger M, Schram C, De Santana L. Reduction of Airfoil Turbulence-Impingement Noise by Means of Leading-Edge Serrations and/or Porous Material. *19th AIAA/CEAS Aeroacoustics Conf*. 2013:1-20. doi:10.2514/6.2013-2108

[3] Clair V, Polacsek C, Le Garrec T, Reboul G, Gruber M, Joseph P. Experimental and Numerical Investigation of Turbulence-Airfoil Noise Reduction Using Wavy Edges. *AIAA J*. 2013;51(11):2695-2713. doi:10.2514/1.J052394

[4] Paruchuri C, Joseph P, Ayton LJ. On the superior performance of leading edge slits over serrations for the reduction of aerofoil interaction noise. *2018 AIAA/CEAS Aeroacoustics Conf*. 2018:1-17. doi:10.2514/6.2018-3121

[5] Roger M, Moreau S. Airfoil Turbulence-Impingement Noise Reduction by Porosity or Wavy Leading-Edge Cut : Experimental Investigations. *Inter-Noise 2016*. 2016;(2):6006-6015.

[6] Chaitanya P, Joseph P, Narayanan S, et al. Performance and mechanism of sinusoidal leading edge serrations for the reduction of turbulence-aerofoil interaction noise. *J Fluid Mech*. 2017;818:435-464. doi:10.1017/jfm.2017.141

[7] Kim JW, Haeri S, Joseph PF. On the reduction of aerofoil-turbulence interaction noise associated with wavy leading edges. *J Fluid Mech*. 2016;792:526-552. doi:10.1017/jfm.2016.95

[8] Bampanis G, Roger M. Three-dimensional effects in the reduction of turbulence-impingement noise of aerofoils by wavy leading edges. 2018;1.

[9] Ayton LJ, Kim JW. An analytic solution for the noise generated by gust–aerofoil interaction for plates with serrated leading edges. *J Fluid Mech*. 2018;853:515-536. doi:10.1017/jfm.2018.583

[10] Piet J-F, G.Elias. Modelisation du champ acoustique incident sur la coiffe d'ariane 5 par des sources simples. 1994.

[11] Avallone F, Prï¿½bsting S, Ragni D. Three-dimensional flow field over a trailing-edge serration and implications on broadband noise. *Phys Fluids*. 2016;28(11). doi:10.1063/1.4966633

[12] Scarano F. Tomographic PIV: Principles and practice. *Meas Sci Technol*. 2013;24(1). doi:10.1088/0957-0233/24/1/012001

2.8. ESR 13: CFD-CAA analysis & optimization methods, with industrial applications

During the last decades there has been tight regulation for noise pollution which shows the importance of an effective noise source mitigation strategy. For example, based on the report FLIGHTPATH2050 of the European Commission [1], it is mandated to reduce the perceived noise level by 65 percent from the level in 2000 by the year 2050. This means that designers must investigate innovative methods in design and optimization fields to further improve the process of designing quieter and more efficient systems. Due to the costly nature of optimization problems, numerical methods have always been of interest. Particularly, of interest are adjoint-based optimization methods [2][3], because the computational cost is independent of the number of design variables that provides an opportunity for researchers for high-fidelity analysis in more practical and complicated problems such as aerodynamics.

Although adjoint methods have a strong background in aerodynamic shape optimization [4], they are relatively new in the field of aeroacoustic optimization. In [5], NTUA presented a continuous adjoint method for the reduction of the noise perceived by the car driver due to its side mirror. However, a steady flow model was used and a turbulence-based surrogate objective functions. This is important to note that without differentiating the turbulence model, i.e. by using the so-called "frozen turbulence assumption", such an optimization could never be solved since the sensitivity derivatives would be equal to zero. Recently, discrete adjoint to hybrid solvers (CFD and FW-H analogy) [6][7][7][9] were developed to reduce the far-field noise of an airfoil or other bodies; however, in all these works, discrete adjoint was used with the help of an automatic differentiation tool. In [10] permeable FW-H formulation in the wave equation form is solved using a finite element method (FEM) instead of integral solution. This led to need of cumbersome derivations of new adjoint boundary conditions at the interface between the CFD and CAA domains while it can be avoided by using integral solution as it will be shown in this work. The implementation of the continuous adjoint for hybrid solver is rare [11], and this has been done with incompressible flow models and the Kirchhoff integral. The extension of the continuous adjoint method to compressible flows based on the FW-H analogy appears in this work and is absolutely new.

2.8.1. Methodology

The origin of hybrid methods in aeroacoustic can be traced back to the Lighthill analogy[12][13]. This formulation later was improved by Curle [14] by including the presence of stationary solid surface and later it was generalized by Ffowcs Williams & Hawkings (FW-H) [15].

In this work, a CFD solution is performed using the in-house GPU based flow solver of PCOpt/NTUA [16][17] which also includes a continuous adjoint solver. A hybrid aeroacoustic noise prediction tool is added to the flow solver based on the permeable version of the FW-H analogy. Then the continuous adjoint formulation for the coupled CFD-CAA solver has been developed on the in-house solver.

The FW-H formulation can be written in laboratory frame by applying a Galilean transformation. For 3D flows there are different solutions to FW-H equation in time domain based on the boundary integral formulation, while solving the FW-H equation in time domain for two dimension leads to tail effect that requires an infinitely long time integration range. This can be tackled by solving the FW-H equation in the frequency domain. The Fourier transformed FW-H equation can be written as following[18] :

$$\left(\frac{\partial^2}{\partial y_i \partial y_i} + k^2 - 2iM_i k \frac{\partial}{\partial y_i} - M_i M_j \frac{\partial^2}{\partial y_i \partial y_j}\right)\left(H(f)\hat{p}'(y,\omega)\right) = \frac{\partial}{\partial y_i}(\hat{F}_i(y,\omega)\delta(f)) - i\omega\hat{Q}(y,\omega)\delta(f) - \frac{\partial^2}{\partial y_i \partial y_j}(\hat{T}_{ij}(y,\omega)H(f)) \tag{1}$$

In (1), the FW-H surface is defined by a function, $f = 0$ such that positive and negative values of f correspond to the outside and inside of the surface respectively. $H(f)$, is the Heaviside function which is 1 for positive values of f and zero for negative. δ is the Dirac delta function and the wave number $k = \omega / c_0$. $\hat{Q}, \hat{F}$ and $\hat{T}_{ij}$ represent the monopole, dipole and quadrupole source terms respectively in the frequency domain and their time-domain counterparts are:

$$Q(y_s,t) = (\rho u_i - \rho_0 U_i)n_i \tag{2}$$

$$F_i(y_s,t) = (\rho(u_i - 2U_i) + \rho U_i U_j + p\delta_{ij} - \tau_{ij})n_j \tag{3}$$

$$T_{ij}(y_s,t) = \rho(u_i - U_i)(u_j - U_j) + (p - c_0^2\rho)\delta_{ij} \tag{4}$$

where $\rho = \rho_\infty + \rho', p = p_\infty + p'$ and $u_i = U_i + u_i'$. Free-stream quantities and mean flow velocity are indicated by subscript ∞ and U_i, respectively. The unit outward normal to surface $f = 0$ is indicated by n. Equation (1) can be solved using the Green function for 2D problems, as:

$$H(f)\hat{p}'(y_o,\omega) = -\iint_{f=0} \hat{F}_i(y_s,\omega)\frac{\partial G(y_o,y_s,\omega)}{\partial y_{is}}ds - \iint_{f=0} i\omega\hat{Q}(y_s,\omega)G(y_o,y_s,\omega)ds - \iiint_{f>0} \hat{T}_{ij}(y_s,\omega)\frac{\partial^2 G(y_o,y_s,\omega)}{\partial y_{is}\partial y_{js}}dV \tag{5}$$

The Green function for flows with Mach number below 1 is defined by:

$$G(y_o,y_s,\omega) = \frac{i}{4\beta}\exp(iMk\bar{x}/\beta^2)H_0^{(2)}\left(\frac{k}{\beta^2}\sqrt{\bar{x}^2 + \beta^2\bar{y}^2}\right) \tag{6}$$

where y_o, y_s are the observer and source positions (nodes on the FW-H surface), $\bar{x} = (\bar{y}_{1o} - \bar{y}_{1s})\cos\theta + (\bar{y}_{2o} - \bar{y}_{2s})\sin\theta$ and $\bar{y} = -(\bar{y}_{1o} - \bar{y}_{1s})\sin\theta + (\bar{y}_{2o} - \bar{y}_{2s})\cos\theta$. The angle θ is mean flow angle such that $\tan\theta = V/U$ and V and U are mean flow velocity in the Y and

X directions, respectively. The Mach number is $M = \sqrt{U^2 + V^2}/c_0$ and the Prandtl-Galuert factor is $\beta = \sqrt{1 - M^2}$. $H_0^{(2)}$ stands for Hankel function of the second kind of zero order.

For the test cases of this work the contribution of quadrupole is negligible. Neglecting quadrupole terms also avoids a huge computational effort of taking a volume integral.

A Hanning window is applied on the source terms before transferring them to frequency domain. More details about implementation of FW-H integral can be found in [18].

2.8.2. Current results

- **Validation of hybrid CFD/FW-H solver**

Three cases are presented in order to verify the hybrid solver. In the first case, results of FW-H solver are compared to a well-known analytical solution of the sound field from a monopole source in uniform flow. This test case is similar to the one used in [18]. Figure 30 compares the directivity at radius of r=500 from both methods and as it can be seen the agreement is excellent, demonstrating that the two-dimensional FW–H formulation is verified for problems with a uniform mean flow.

In the second case, a comparison between the FW–H result and the outcome of a CFD simulation is performed. A NACA12 airfoil is pitching in an inviscid flow around the zero angle of attack while the amplitude of pitching is 1.01 deg and the period of pitching is 0.114 sec. The Mach number is 0.4 and the simulation was run with 40 time steps per period. A 2D unstructured grid which extends to 50 chords away from the airfoil is used, with 51000 nodes overall, among which 202 nodes are on airfoil and 151 nodes on the FW-H surface. FW-H surface is placed at radius of 5 chords. Directivity pattern for an observer at radius of 20 chords is plotted in Figure 31, which shows the good agreement between results of direct CFD and FW-H integral. In this case, a non-reflecting far-field condition was also applied which enhances the direct CFD result considerably as it can be seen in Figure 31; however, results of the FW-H integral method remains almost the same. This is due to the fact that the FW-H surface is placed in a safe area so is not affected by reflection.

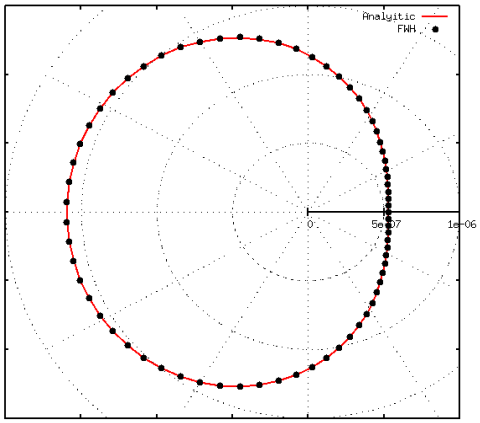

Figure 30: Directivity plot of a monopole in flow

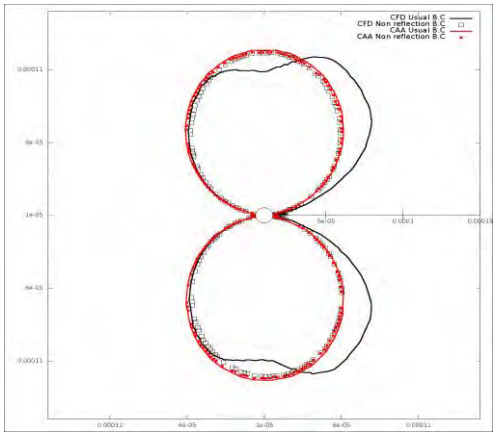

Figure 31: Directivity plot of a pitching airfoil

The third test case for the coupled CFD/CAA solver is a 2D cylinder in laminar flow which undergoes vortex shedding. The Mach and Reynolds number are 0.2 and 1000, respectively. The Strouhal number is 0.164 and the grid is structured with 310 nodes along the cylinder and 150 nodes in the radial direction. 10 periods of shedding have been included in the time window. Different positions for the integration surface have been tested. As it is shown in Figure 32, directivity patterns from the FW-H integral are matched with direct CFD results for an observer at radius of 10 D (diameter of cylinder). Some of the discrepancies seen are caused by neglecting the quadrupole terms in formulation and the passage of vortices through the FW-H surface, as results are improved in case of integration surface on the cylinder. However, propagation errors in CFD/CAA solution affect the accuracy of solution as well.

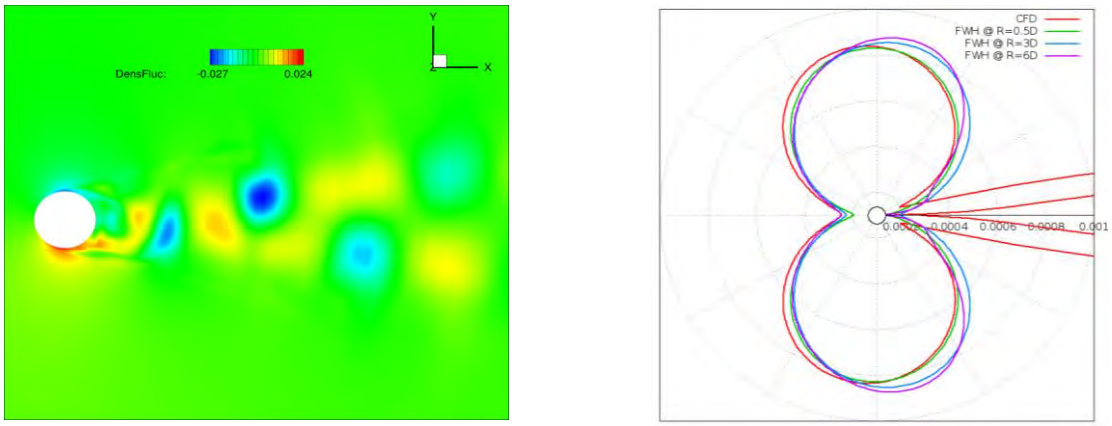

Figure 32: (Left) Contour of density fluctuation, (Right) Directivity plot for observer at R=10D and FW-H surface at different position.

- **Unsteady adjoint**

In aerodynamic shape optimization, adjoint methods compute or approximate the gradient of an objective function with respect to design variables. First, a system of adjoint equations has to be formulated by taking into consideration the governing equations. Second step is solving the adjoint equations at a cost which is practically independent of the number of design variables.

An aerodynamic shape optimization for the lift coefficient has been performed firstly. The case is exactly the same as the pitching NACA12 airfoil in previous section. The airfoil is parameterized using 16 Bezier control points. Figure 33 shows how the lift force has increased from its initial value, zero (pitching around zero angle of attack) after 5 optimization cycles, by changing the shape basically at trailing edge.

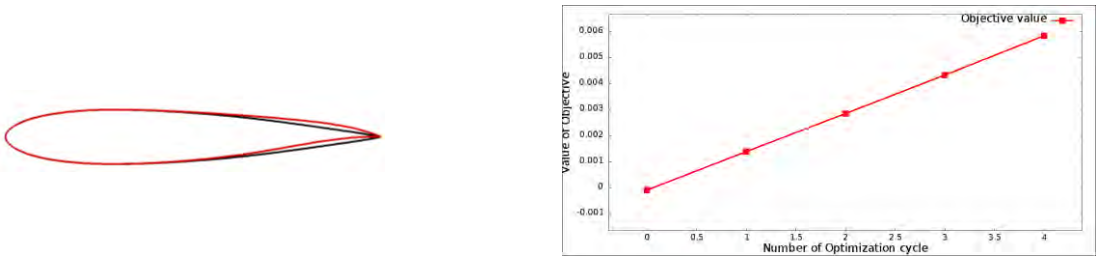

Figure 33: Initial and final shapes in black and red, respectively (Left). Objective function, i.e. lift, values (Right).

In the continuous adjoint method formulation for CFD/CAA problems, it can be shown that the contribution of CAA part in adjoint equations is in form of source terms lying over the integration surface. An appropriate objective function J can be defined and differentiated as following:

$$J = \int_{freq} \left|\hat{P}'\right|^2 \, \mathrm{df} \tag{7}$$

$$\frac{\delta J}{\delta b_n} = -\int_T \int_{S=0} \left[\int_{freq} \left((A+B) d\omega \frac{\delta \hat{F}_k}{\delta b_n} \right) + \int_{freq} \left(\omega (C+D) d\omega \frac{\delta \hat{Q}}{\delta b_n} \right) \right] dS \; dt$$

where,

$$A = \left(\hat{P}'_{\mathrm{Re}} \left(\frac{\partial \hat{G}}{\partial x_k} \right)_{\mathrm{Re}} + \hat{P}'_{\mathrm{Im}} \left(\frac{\partial \hat{G}}{\partial x_k} \right)_{\mathrm{Im}} \right) \left(Han(t) \cos(2\pi\omega t) - Han\cos(\omega) \right)$$

$$B = \left(\hat{P}'_{\mathrm{Re}} \left(\frac{\partial \hat{G}}{\partial x_k} \right)_{\mathrm{Im}} - \hat{P}'_{\mathrm{Im}} \left(\frac{\partial \hat{G}}{\partial x_k} \right)_{\mathrm{Re}} \right) \left(Han(t) \sin(2\pi\omega t) - Han\sin(\omega) \right) \tag{8}$$

$$C = \left(\hat{P}'_{\mathrm{Im}} \hat{G}_{\mathrm{Re}} - \hat{P}'_{\mathrm{Re}} \hat{G}_{\mathrm{Im}} \right) \left(Han(t) \cos(2\pi\omega t) - Han\cos(\omega) \right)$$

$$D = \left(\hat{P}'_{\mathrm{Im}} \hat{G}_{\mathrm{Im}} - \hat{P}'_{\mathrm{Re}} \hat{G}_{\mathrm{Re}} \right) \left(Han(t) \sin(2\pi\omega t) - Han\sin(\omega) \right)$$

where,

$$Han\cos(\omega) = \frac{1}{T} \int_T Han(t) \mathrm{Cos}(2\pi\omega t) dt \quad \text{and,} \quad Han\sin(\omega) = \frac{1}{T} \int_T Han(t) \mathrm{Sin}(2\pi\omega t) dt$$

$Han(t)$ stands for the Hanning window and subscripts Im and Re refer to the real and imaginary part of complex variables.

2.8.3. Conclusions and outlook

The unsteady continuous adjoint solver developed at NTUA is modified to include the coupled CFD/CAA problems. The solver was initially programmed for a variety of objective functions such as the lift or drag as well as for optimization in internal aerodynamics. As mentioned in the previous section, the CAA contributes source terms to the adjoint equations according to

equation (8) while it does not affect the boundary condition or sensitivity derivatives. By applying the required changes in the code, the solver is ready to perform optimization for noise reduction. The first case will be the pitching NACA12 airfoil with an inviscid fluid. The accuracy of the solver will be validated by comparing the sensitivity derivatives calculated by continuous adjoint solver to that from finite difference.

2.8.4. References

[1] Darecki, M., et al. "Flightpath 2050 Europes Vision for Aviation." Off. Eur (2011).

[2] Pironneau, O. “On optimum design in fluid mechanics.” Journal of Fluid Mechanics 64, 97–110, 1974.

[3] Jameson, “A. Aerodynamic design via control theory”. Journal of Scientific Computing 3, 233–260, 1988.

[4] Papoutsis-Kiachagias, E. M., & Giannakoglou, K. C. “Continuous adjoint methods for turbulent flows, applied to shape and topology optimization: Industrial applications”. Archives of Computational Methods in Engineering, 23(2), 255-299. 2016

[5] Papoutsis-Kiachagias, E. M., et al. "Noise reduction in car aerodynamics using a surrogate objective function and the continuous adjoint method with wall functions." Computers & Fluids 122 (2015): 223-232.

[6] Rumpfkeil, M. P. and Zingg, D. W. “A hybrid algorithm for far-field noise minimization. Computers and Fluids″ 39(9), 1516–1528. 2010

[7] Zhou, B. Y., Albring, T., Gauger, N. R., Economon, T. D., Palacios, F., & Alonso, J. J. (2015). A discrete adjoint framework for unsteady aerodynamic and aeroacoustic optimization. AIAA Paper, 3355, 2015.

[8] Zhou, Beckett Y., Tim Albring, Nicolas R. Gauger, Carlos R. Ilario da Silva, Thomas D. Economon, and Juan J. Alonso. “An Efficient Unsteady Aerodynamic and Aeroacoustic Design Framework Using Discrete Adjoint.” In 17th AIAA/ISSMO Multidisciplinary Analysis and Optimization Conference, p. 3369. 2016.

[9] Zhou, Beckett, et al. "Reduction of Airframe Noise Components Using a Discrete Adjoint Approach." 18th AIAA/ISSMO Multidisciplinary Analysis and Optimization Conference. 2017.

[10] Economon, T. D., Palacios, F., & Alonso, J. J. “A coupled-adjoint method for aerodynamic and aeroacoustic optimization.” AIAA paper, 5598, 2012.

[11] Kapellos, C. The continuous adjoint method for automotive aeroacoustic shape optimization, PhD Thesis, NTUA, to be integrated in 2019.

[12] Lighthill, M. J. “On sound generated aerodynamically. I. General theory.” Proc. R. Soc. Lond. A 211, 564–587, 1952.

[13] Lighthill, M. J. “On sound generated aerodynamically. II. Turbulence as a source of sound.” Proc. R. Soc. Lond. A 222, 1–32, 1954.

[14] Curle, N. “The influence of solid boundaries upon aerodynamic sound.” Proc. R. Soc. Lond. A 231, 505–514. 1955

[15] Ffowcs Williams, J. E. & Hawkings, D. “Sound generation by turbulence and surfaces in arbitrary motion.” Phil. Trans. R. Soc. Lond. A 264, 321–342. 1969.

[16] I.C. Kampolis, X.S Trompoukis, V.G. Asouti and K.C. Giannakoglou. CFD-based analysis and two-level aerodynamic optimization on Graphics Processing Units. Computer Methods in Applied Mechanics and Engineering 2010; 199(9-12):712-722.

[17] V.G. Asouti, X.S Trompoukis, I.C. Kampolis and K.C. Giannakoglou. Unsteady CFD computations using vertex-centered finite volumes for unstructured grids on Graphics Processing Units. International Journal for Numerical Methods in Fluids 2011; 67(2):232-246.

[18] Lockard, David P. "An efficient, two-dimensional implementation of the Ffowcs Williams and Hawkings equation." Journal of Sound and Vibration 229, no. 4 (2000): 897-911.

2.9. ESR 16: Reduction of the broadband noise of centrifugal fans used on HVAC in buildings

2.9.1. Review on state-of-the-art

- **Leading edge serrations**

Since [1], leading edge serrations have proven to be an efficient means to reduce turbulent interaction noise. The following noise reduction mechanisms have been identified:

- Destructive interference of the scattered surface pressure [2], [3]
- Cutoff effect due to the oblique edge [4]
- Stall delay (indirect effect) [5], [6]

In [7] it was shown that the use of complex leading-edge serrations, with double wavelength, chopped-peak, slitted-root and slitted-V, can produce greater noise reductions than single wavelength serrations.

In [8], a noise reduction of 3 dB over 1 kHz was measured on a NACA 65 airfoil. It was proposed that $\lambda/2 = l_y$ (correlation scale) and that 2h should be as big as possible without hindering the aerodynamics. It has been shown in [9] the existence of an optimum serration angle, $\theta_0=\tan^{-1}(2h/\Lambda)$, function of the turbulence integral length scale Λ. In [10] an optimum was found for $\lambda_0=4\ \Lambda_{transverse}$, at which compact sources at adjacent valleys are excited incoherently.

In [11] it was achieved a maximum reduction of 11 dB at 4300-4500 Hz with sinusoidal leading edge on a NACA-0003. Measurements off the midspan plane showed that noise reduction can be larger at 75º at lower frequencies, and validated Amiet's model for arbitrary radiation directions.

Some analytical models have also been developed. For example, [12] studied noise reduction on a NACA-12 airfoil, and proposed a new analytical model by extending Amiet's theory to a serrated leading edge. More recently, [13] generalized Amiet's theory for a flat plate with a serrated leading edge.

In [14], serrations were added to the leading edge of the blades of an axial fan. The results showed a reduction in low-frequency broadband and tonal components. In [15] both single and double-sine serrations on the LE of an axial fan were tested, with the former being more efficient than the latter. In [6] serrations were added to the leading edge of an axial fan. A maximum noise reduction of 13 dB was achieved for a certain configuration (but it also increased noise up to 3 dB at other operating points).

- **Trailing edge serrations**

Whereas the study of leading edge serrations started in the 1970s, the study of trailing edge serrations did not start until the late 1980s. In [16], [17], Howe developed an analytical model for the potential self-noise reduction on a flat plate. Experiments partially validated the theory, but the results have never fully achieved the predictions, and a noise increase at high frequencies can even appear. In [18] reductions up to 5-10 dB were achieved on flat plates and airfoils, showing

that the alignment of the plane of the serrations with the trailing-edge flow is critical to reduce the noise increase. The applications of the same serrations to wind turbines (see [19]) only yielded partial results, with a maximum noise reduction of 3.5 dB and noise increase at higher frequencies. A similar trend was observed by [20], with noise reduction up to 5 dB under 1 kHz, but a noise increase over this threshold. In [21], serrations were directly carved in an airfoil, achieving reductions up to 30 dB in laminar regime and 6.5 dB with a turbulent flow (but generating vortex shedding noise at high frequency).

The following noise reduction mechanisms have been identified:

- Reduction of spanwise correlation associated with sound radiation [16], [17]
- Influence on hydrodynamic field at source location [22]
- Vortex shedding suppression [22], [23]

Some progress has also been done on analytical modelling. In [24], Howe's model was extended to slitted trailing edges. In [25], a new analytical method, more realistic and consistent than Howe's, was developed.

Other serration geometries have been assessed. In [26], a parametric study was carried out with rectangular silts, serrations with holes, slitted sawtooth and random slits. In [27], three different shapes were compared: triangular, trapezoidal and wishbone.

In [28], serrations were added to the trailing edge of an UAV propeller. Broadband noise reduction was achieved at low frequencies, but the aerodynamic performance of the propeller was degraded (and noise increase was observed at certain angles). Polar measurements show that noise reduction is highly directional.

2.9.2. Summary of present activities

- **Test of baseline fan**

Two series of tests were carried out in June and September 2018 in order to characterize the aerodynamics and acoustics of the baseline fan. The fan total pressure curve was obtained at 100% of the nominal speed (1440 rpm), 75% (1080 rpm) and 50% (720 rpm).

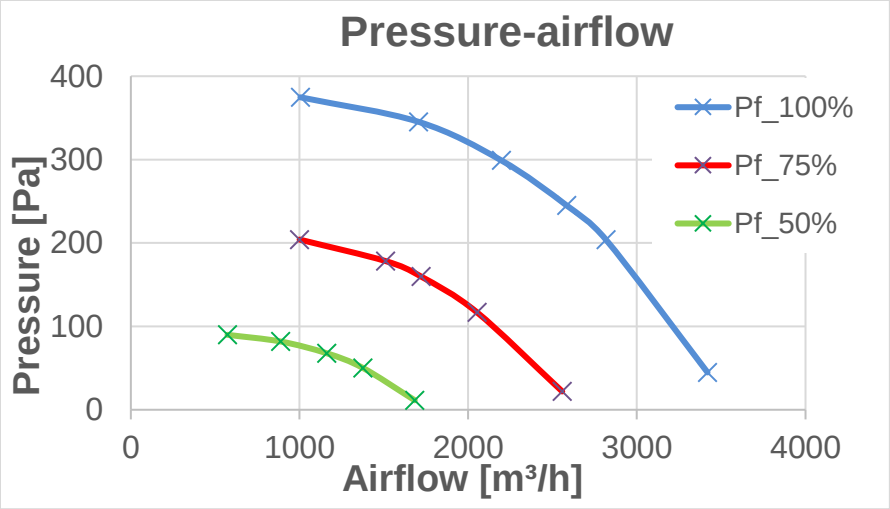

Figure 34: Pressure-flow curve of the fan at different rotating speeds

At each operating point the noise was measured at both the inlet and the outlet. The data was presented as sound power, sound power in third-octave bands and broadband sound pressure level. The following Figure 35 shows the A-weighted overall sound power with $\delta = q/US$, where U=πDN and S=πDL.

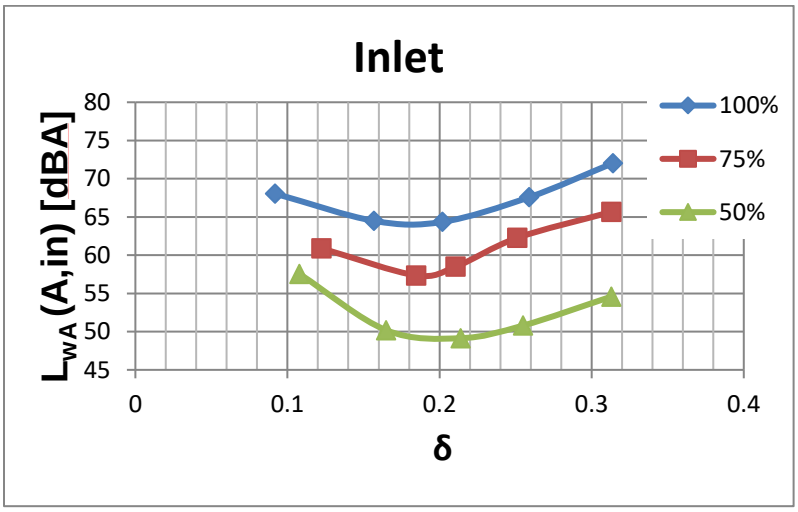

Figure 35: Overall sound power vs the dimensionless flow

The following conclusions can be drawn from the analysis of the data from the tests:

- The baseline fan is quite silent when compared to fans of the same type. This will allow us to validate the noise reduction techniques on a well-optimized impeller.
- The similarity laws have been verified at the three rotating speeds for both the aerodynamics and the acoustics.
- Different hypothesis have been proposed to identify some of the peaks and narrowband areas of the broadband SPL plots: motor noise, laminar bubble instability, resonances…

- **CFD simulations**

A series of CFD simulations were carried out to gain a better insight on the flow morphology between the fan blades. The conditions and geometry of the test rig were replicated with the commercial software Star CCM +. Three operating points were reproduced: the BEP (best efficiency point, at 2196 m^3/h) and the points right and left of it. The prediction of the air performance, which used the RANS equations and the k-ε turbulence model, showed quite a good agreement with the measurements, albeit a certain underprediction of the pressure.

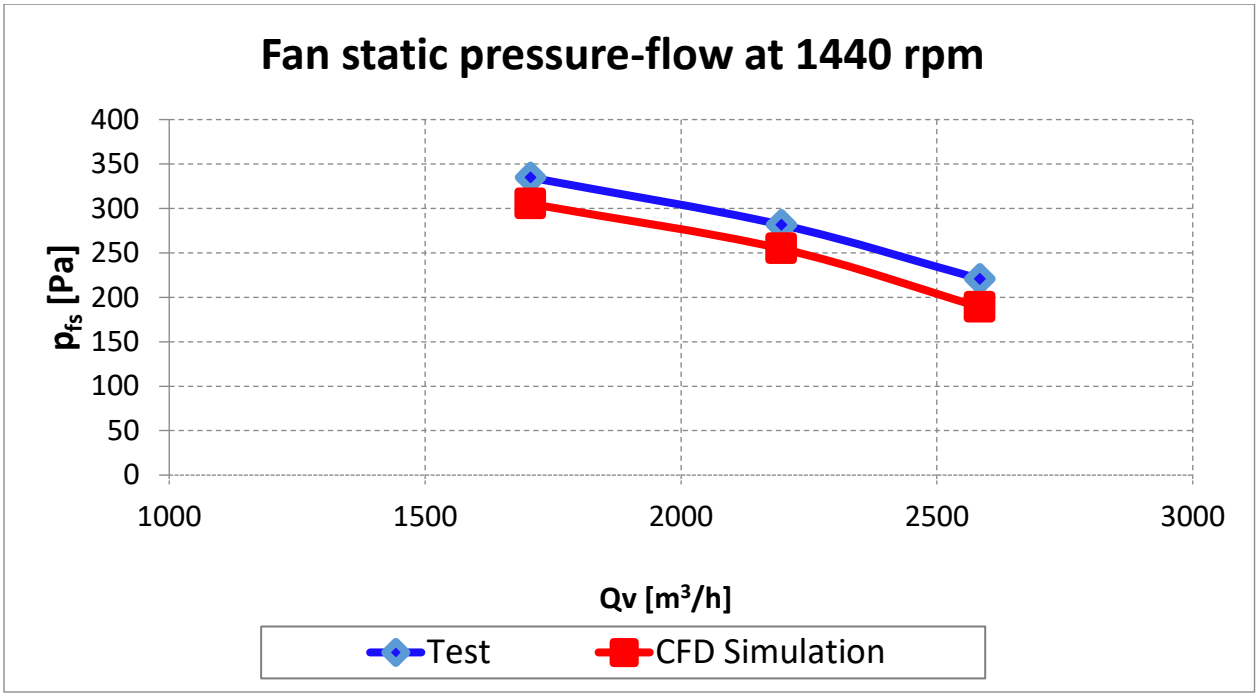

Figure 36: Comparison of the fan pressure curves of the tests and the simulations

A transversal section through the middle plane will give us a good insight on the flow characteristics:

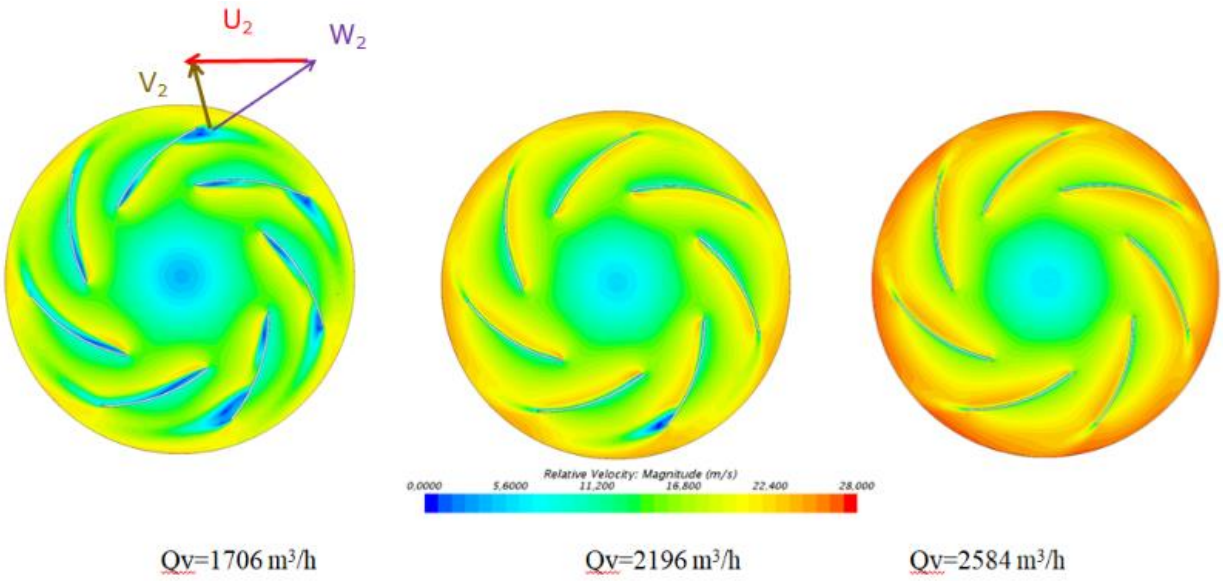

Figure 37: relative velocity magnitude (W_2) on the middle plane of the impeller, for three values of Q_v (1706 m^3/h on the left, 2196 m^3/h on the middle and 2584 m^3/h on the right)

The relative velocity field in the plane between two blades can complement the previous information. We can better appreciate how the flow direction changes from spanwise at the inlet to chordwise at the outlet.

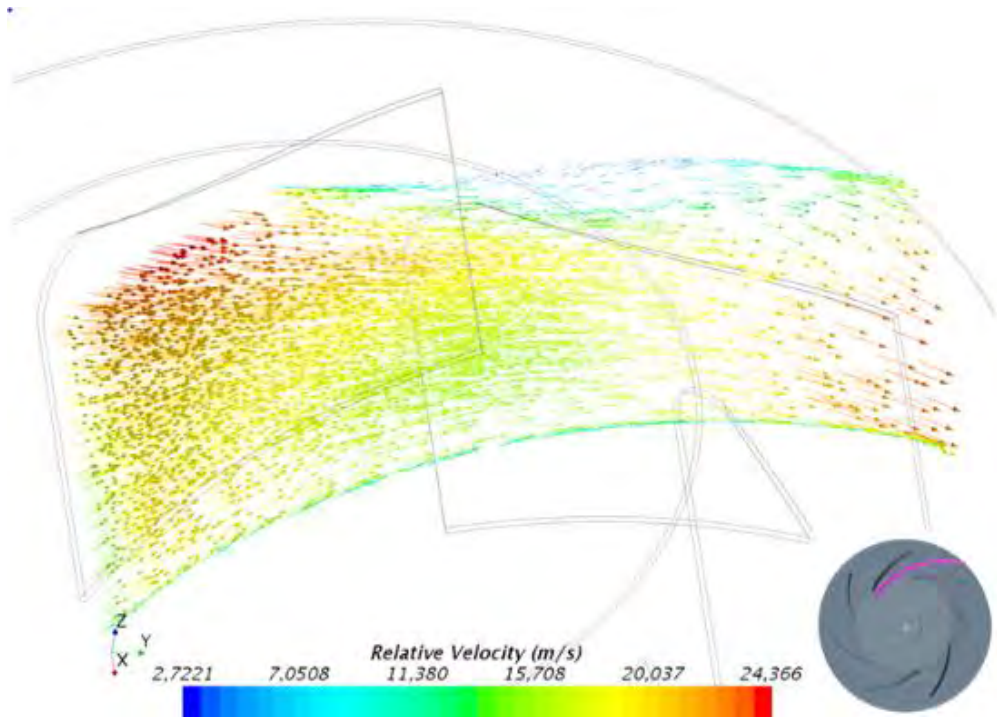

Figure 38: Relative velocity vectors between two blades

The analysis of the outcome of the simulations yields the following conclusions:

- There is a good flow guiding between the blades at the BEP, despite some flow separation on the suction side (which grows when the flow is reduced).
- There is a recirculation area over the front plate due to the inability of the flow to adequately follow its shape.
- The boundary layer has a thickness of around 0.5 mm on the pressure side of the blade and 2 mm on the suction side.
- The integral turbulent length scale upstream of the leading edge has been estimated at around 8 mm.

- **Design of prototypes**

Three impeller prototypes with a serrated leading edge have been designed:

Name	Wavelength λ [mm]	Amplitude (2h) [mm]
LE_L8H11	8	22
LE_L16H11	16	22
LE_L16H22	16	44

This will allow us to do a parametric study on both the wavelength and the amplitude, and to assess the validity of the application to fans of the results for airfoils. The wavelength of 16 mm has been set based on the optimum criterion from [9], while the amplitude has taken a value of 1/3 and 1/6 of the chord- a usual ration in the bibliography. The prototypes will be manufactured in partnership with Ziehl-Abegg SE, and are expected to be delivered in February 2019.

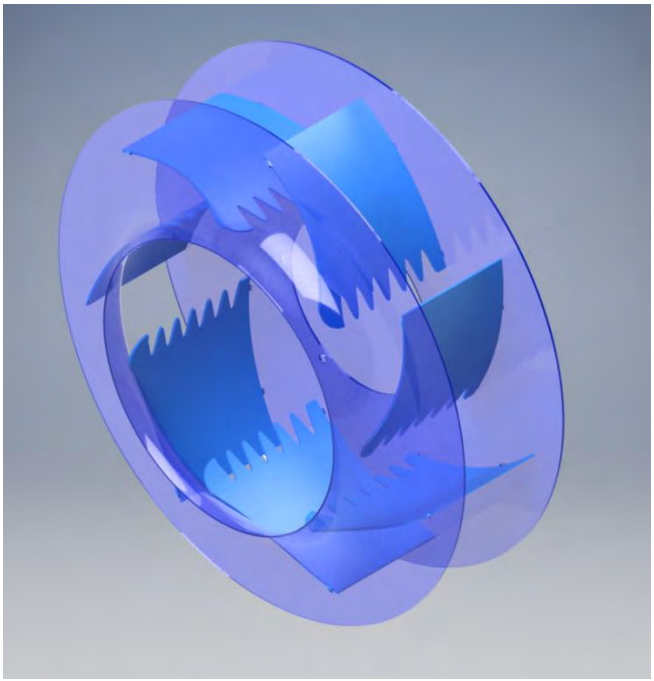

Figure 39 Rendering of the impeller LE_L16H11

2.9.3. Preliminary conclusions and outlook

In the previous months, a thorough bibliography analysis was performed. This has allowed to identify serrations as the main noise reduction method to be tested during the research project. The tests of the baseline fan have allowed us to do a diagnosis of its aerodynamics and acoustics. This information will be used to evaluate the impact of the modifications on the performance of the impeller. The CFD simulations are an excellent complement of the experiments, and have allowed us to gain a better understanding of the flow field.

Based on the state-of-the-art, three impellers with leading edge serrations have been designed. They will be tested to assess the impact of the new geometry, and this outcome will allow us to design a second series of prototypes. At the same time, the possibility to design an impeller with serrated trailing edge will be evaluated.

As part of the collaboration within the SmartAnswer consortium, a secondment in École Centrale de Lyon started in October 2018. The main objective will be the adaptation of Amiet's analytical model to a centrifugal fan. Given the geographical proximity of ECL, it has been decided to divide the planned duration of one month into different sessions to adapt to the needs and constraints of the main research activity.

Another secondment in the company Valeo is also planned for two weeks of 2019, but the final dates are yet to be decided. The objective will be to pursue the analysis of the CFD simulations and to perform some acoustic studies based on them.

2.9.4. References

[1] P. T. Soderman, “Leading edge serrations which reduce the noise of low-speed rotors,” *NASA Tech. Note*, 1973.

[2] S. Narayanan, P. Chaitanya, S. Haeri, P. Joseph, J. W. Kim, and C. Polacsek, “Airfoil noise reductions through leading edge serrations,” *Phys. Fluids*, vol. 27, no. 2, 2015.

[3] B. Lyu, M. Azarpeyvand, and S. Sinayoko, “Noise Prediction for Serrated Leading-edges,” *22nd AIAA/CEAS Aeroacoustics Conf.*, 2016.

[4] J. W. Kim, S. Haeri, and P. Joseph, “On the reduction of aerofoil-turbulence interaction noise associated with wavy leading edges,” *J. Fluid Mech.*, vol. 792, pp. 526–552, 2016.

[5] A. Corsini, G. Delibra, and A. G. Sheard, “The application of sinusoidal blade-leading edges in a fan-design methodology to improve stall resistance,” *Proc. Inst. Mech. Eng. Part A J. Power Energy*, vol. 228, no. 3, pp. 255–271, 2014.

[6] T. Biedermann, N. Hintzen, F. Kameier, T. P. Chong, and C. O. Paschereit, “On the Transfer of Leading Edge Serrations from Isolated Aerofoil to Ducted Low-Pressure Fan Application,” *2018 AIAA/CEAS Aeroacoustics Conf.*, 2018.

[7] P. Chaitanya, S. Narayanan, P. Joseph, and J. W. Kim, “Leading edge serration geometries for significantly enhanced leading edge noise reductions,” *22nd AIAA/CEAS Aeroacoustics Conf.*, no. August, 2016.

[8] V. Clair, C. Polacsek, T. Le Garrec, G. Reboul, M. Gruber, and P. Joseph, "Experimental and Numerical Investigation of Turbulence-Airfoil Noise Reduction Using Wavy Edges," *AIAA J.*, vol. 51, no. 11, pp. 2695–2713, 2013.

[9] P. Chaitanya *et al.*, "Broadband noise reduction through leading edge serrations on realistic aerofoils," *21st AIAA/CEAS Aeroacoustics Conf.*, no. June, pp. 1–29, 2015.

[10] P. Chaitanya *et al.*, "Performance and mechanism of sinusoidal leading edge serrations for the reduction of turbulence-aerofoil interaction noise," *J. Fluid Mech.*, vol. 818, pp. 435–464, 2017.

[11] G. Bampanis and M. Roger, "Three-dimensional effects in the reduction of turbulence-impingement noise of aerofoils by wavy leading edges," *Euronoise 2018*, vol. 1, 2018.

[12] M. Roger, C. Schram, and L. De Santana, "Reduction of Airfoil Turbulence-Impingement Noise by Means of Leading-Edge Serrations and / or Porous Materials," *19th AIAA/CEAS Aeroacoustics Conf.*, pp. 1–20, 2013.

[13] B. Lyu and M. Azarpeyvand, "On the noise prediction for serrated leading edges," *J. Fluid Mech.*, vol. 826, pp. 205–234, Sep. 2017.

[14] F. Zenger, A. Renz, and S. Becker, "Experimental Investigation of Sound Reduction by Leading Edge Serrations in Axial Fans," *23rd AIAA/CEAS Aeroacoustics Conf.*, no. June, pp. 1–13, 2017.

[15] F. Krömer, M. Westermeier, A. Renz, S. Becker, and F. Alexander, "Sound reduction by leading edge serrations in low-pressure axial fans," in *Fan 2018*, 2018, no. Figure 1, pp. 1–12.

[16] M. S. Howe, "Noise produced by a sawtooth trailing edge," *J. Acoust. Soc. Am.*, vol. 90, no. 1, pp. 482–487, 1991.

[17] M. S. Howe, "Aerodynamic noise of a serrated trailing edge," *J. Fluids Struct.*, vol. 5, no. 1, pp. 33–45, 1991.

[18] T. Dassen, R. Parchen, J. Bruggeman, and F. Hagg, "Results of a wind tunnel study on the reduction of airfoil self-noise by the application of serrated blade trailing edges," *Proceeding Eur. Union Wind Energy Conf. Exhib.*, no. September, pp. 800–803, 1996.

[19] K. Braun *et al.*, "Serrated trailing edge noise (STENO)," *Proc. Eur. Wind Energy Conf.*, pp. 180–183, 1999.

[20] S. Oerlemans, M. Fisher, T. Maeder, and K. Kögler, "Reduction of Wind Turbine Noise Using Optimized Airfoils and Trailing-Edge Serrations," *AIAA J.*, vol. 47, no. 6, pp. 1470–1481, 2009.

[21] T. P. Chong, A. Vathylakis, P. Joseph, and M. Gruber, "Self-Noise Produced by an Airfoil with Nonflat Plate Trailing-Edge Serrations," *AIAA J.*, vol. 51, no. 11, pp. 2665–2677, 2013.

[22] D. Moreau, L. Brooks, and C. Doolan, "On the noise reduction mechanism of a flat plate serrated trailing edge at low-to-moderate Reynolds number," *18th AIAA/CEAS*

Aeroacoustics Conf. (33rd AIAA Aeroacoustics Conf., no. June, pp. 1–20, 2012.

[23] M. Herr, "Experimental Study on Noise Reduction through Trailing Edge Brushes," in *New Results in Numerical and Experimental Fluid Mechanics V. Notes on Numerical Fluid Mechanics and Multidisciplinary Design (NNFM)*, vol. 92, 2006, pp. 365–372.

[24] M. Gruber, M. Azarpeyvand, and P. Joseph, "Airfoil trailing edge noise reduction by the introduction of sawtooth and slitted trailing edge geometries," *Proc. 20th Int. Congr. Acoust. ICA*, vol. 10, no. August, pp. 1–9, 2010.

[25] B. Lyu, M. Azarpeyvand, and S. Sinayoko, "Prediction of noise from serrated trailing edges," *J. Fluid Mech.*, vol. 793, pp. 556–588, 2016.

[26] M. Gruber, P. Joseph, and M. Azarpeyvand, "An experimental investigation of novel trailing edge geometries on airfoil trailing edge noise reduction," *19th AIAA/CEAS Aeroacoustics Conf.*, p. 10, 2013.

[27] F. M. Catalano and L. D. Santana, "Airfoil self noise reduction by application of different types of trailing edge serrations," *28th Int. Congr. Aeronaut. Sci.*, no. September, 2012.

[28] T. Pagliaroli, R. Camussi, P. Candeloro, O. Giannini, G. Bella, and R. Panciroli, "Aeroacoustic Study of small scale Rotors for mini Drone Propulsion: Serrated Trailing Edge Effect.," *2018 AIAA/CEAS Aeroacoustics Conf.*, pp. 1–13, 2018.